

ZERO-SHOT IMPUTATION WITH FOUNDATION INFERENCE MODELS FOR DYNAMICAL SYSTEMS

Patrick Seifner^{1,2}, Kostadin Cvejoski^{1,3}, Antonia Körner² & Ramsés J. Sánchez^{1,2,3}
 Lamar Institute¹, University of Bonn² & Fraunhofer IAIS³
 sanchez@bit.uni-bonn.de

ABSTRACT

Dynamical systems governed by ordinary differential equations (ODEs) serve as models for a vast number of natural and social phenomena. In this work, we offer a fresh perspective on the classical problem of imputing missing time series data, whose underlying dynamics are assumed to be determined by ODEs. Specifically, we revisit ideas from amortized inference and neural operators, and propose a novel supervised learning framework for *zero-shot time series imputation*, through parametric functions satisfying some (hidden) ODEs. Our proposal consists of two components. First, a broad probability distribution over the space of ODE solutions, observation times and noise mechanisms, with which we generate a large, synthetic dataset of (hidden) ODE solutions, along with their noisy and sparse observations. Second, a neural recognition model that is trained *offline*, to map the generated time series onto the spaces of initial conditions and time derivatives of the (hidden) ODE solutions, which we then integrate to impute the missing data. We empirically demonstrate that *one and the same* (pretrained) recognition model can perform zero-shot imputation across 63 distinct time series with missing values, each sampled from widely different dynamical systems. Likewise, we demonstrate that it can perform zero-shot imputation of missing high-dimensional data in 10 vastly different settings, spanning human motion, air quality, traffic and electricity studies, as well as Navier-Stokes simulations — *without requiring any fine-tuning*. What is more, our proposal often outperforms state-of-the-art methods, which are trained on the target datasets.

Our pretrained model will be available online soon.

1 INTRODUCTION

Dynamical systems are mathematical systems that change with time according to a fixed evolution rule, and serve as representational and analytical tools for phenomena which generate patterns that change over time. Very often, the recorded changes of these empirical patterns are such that they can be viewed as occurring continuously in time, and thus can be represented mathematically by systems whose evolution rule is defined through differential equations. Dynamical systems governed by ordinary differential equations (ODEs) correspond to an important subset of these models, and describe the rate of change of a single parametric function $\mathbf{x} : \mathbb{R}^+ \rightarrow \mathbb{R}^D$, which represents the state of the (D -dimensional) system, as time evolves, by means of a vector field $\mathbf{f} : \mathbb{R}^+ \times \mathbb{R}^D \rightarrow \mathbb{R}^D$. In equations, we write

$$\dot{\mathbf{x}}(t) = \mathbf{f}(t, \mathbf{x}(t)), \text{ where } \dot{\mathbf{x}}(t) = \frac{d\mathbf{x}(t)}{dt}. \quad (1)$$

These deceptively simple systems have had a fundamental role in our understanding of many natural processes across nearly every scientific discipline — from their very introduction and application to celestial mechanics in the late seventeenth century (Newton, 1687; Bernoulli, 1712), to their function as models of concentration changes in molecular reaction networks (Hoff, 1986); models of population oscillations in biology (Lotka, 1925; Volterra, 1927); of atmospheric convection and its chaotic features (Lorenz, 1963); and of the coherent, high energy modes within turbulent flows (Noack et al., 2003), just to name a few — and continue to be the go-to mathematical objects for the representation of dynamic phenomena today.

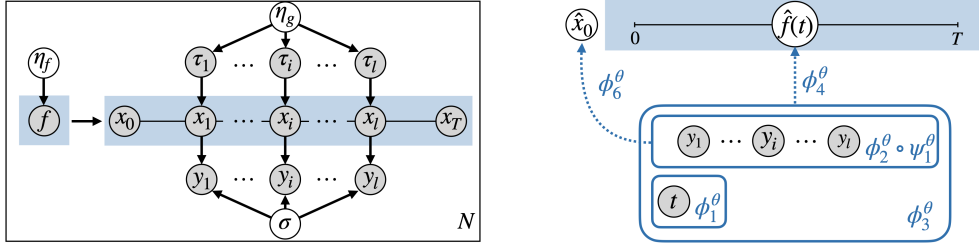


Figure 1: Foundation Inference Model (FIM) for Dynamical Systems. *Left*: Graphical model of the FIM data generation model (Eq. 2). Filled (empty) circles represent observed (unobserved) random variables. The light blue rectangle represents parametric functions. *Right*: Schematic representation of $\text{FIM-}l$, the inference model for interpolating point-wise missing patterns.

In this work, we consider the general problem of imputing missing values in time series data, recorded from some empirical process ($\mathbf{y}^* : \mathbb{R}^+ \rightarrow \mathbb{R}^D$) whose dynamics are *assumed* to be governed by some unknown ODE. In other words, we assume that both available and missing values in the series $\mathbf{y}^*(\tau_1), \dots, \mathbf{y}^*(\tau_l)$ correspond to the values taken by *the solution* $\mathbf{x}(t)$ of some hidden ODE, at the observation times τ_1, \dots, τ_l , potentially corrupted by some noise signal of which only a few statistics are known. Therefore, the goal is to infer the ODE solution $\mathbf{x}(t)$ that best *interpolates* the noisy time series $\mathbf{y}^*(\tau_1), \dots, \mathbf{y}^*(\tau_l)$, and hence *imputes its missing values*.

The current machine learning paradigm tackles this problem by (implicitly) constraining models to handle a single process only. That is, practitioners typically encode their inductive biases into either the model architectures or the training objectives, and optimize the model parameters to fit a single empirical distribution (see *e.g.* Section 2). One disadvantage of this approach is that models trained to fit a single process tend to be overly specific to its distribution, and thus can rarely be reused to impute the missing values of a second one, even when both processes are assumed to *e.g.* be governed by similar ODE. Another disadvantage is that to succeed, the paradigm requires practitioners to have access to enough observations on the process they study, to train and test their models from scratch; and that they also have the experience and expertise to face the trials and tribulations of their intricate training procedures.

In this paper, we instead frame the imputation problem as an instance of *amortized inference*, in the sense introduced by [Stuhlmüller et al. \(2013\)](#). Indeed, in lieu of training one complex model on a single empirical process, we train a neural recognition model *offline* to infer a *large and varied set* of ODE solutions $\mathbf{x}(t)$, from a synthetic dataset that is composed of noisy series of observation on those solutions, displaying different missing value patterns. Somewhat more precisely, we train our model in a supervised fashion, to infer both the (latent) initial conditions $\mathbf{x}(0)$ and (latent) time derivatives $\dot{\mathbf{x}}(t)$ that determine the target set of ODE solutions. However, opposite to [Stuhlmüller et al. \(2013\)](#) and other follow-up works, like that by [Paige & Wood \(2016\)](#), who treat their recognition models as auxiliary to Monte Carlo methods, we employ our pretrained models to directly impute different synthetic, simulation and experimental datasets, *without any parameter fine-tuning*. We therefore adopt the “zero-shot” terminology of [Larochelle et al. \(2008\)](#), by which we mean that our proposal aims to recognize objects (*i.e.* ODE solutions and their time derivatives) whose instances (*i.e.* noisy and sparse time series) may have not been seen during training.

In what follows, we first briefly review previous work on time series imputation in Section 2. Section 3 introduces our main ideas, the synthetic dataset encoding our assumptions, and our recognition model, which we name *Foundation Inference Model*¹ (FIM) for dynamical systems. In Section 4, we report our experimental findings and empirically demonstrate that: (i) the hierarchical structure underlying FIM — which treats $\mathbf{x}(0)$ and $\dot{\mathbf{x}}(t)$ as latent variables — allows us to reconstruct, in a zero-shot fashion, the phase portrait of complex dynamical systems; (ii) FIM is able to impute, in zero-shot mode, missing values in a set of 63 noisy time series, each of which is sampled from dynamical systems of different dimensionalities, and outperform state-of-the-art models which are

¹We choose to name our model foundation model because it goes in line with the definition proposed by [Bommasani et al. \(2021\)](#). To wit: a foundation model is any model that is trained on broad data (generally using self-supervision at scale) that can be adapted to a wide range of downstream tasks.

trained on these datasets; and (iii) the same (pretrained) FIM can perform zero-shot imputation of vastly different, high-dimensional, experimental and simulation data, while often out-performing state-of-the-art models which, again, are trained on the target datasets. Finally, Section 5 comments on the main limitations of our methodology, and closes the paper with some concluding remarks about future work.

2 RELATED WORK

In its most general form, the problem of imputing missing time series data with an ODE model involves inferring the vector field ($\mathbf{f} : \mathbb{R}^+ \times \mathbb{R}^D \rightarrow \mathbb{R}^D$) that defines the (hidden) ODE in question. In some applications, the functional form of the vector field can be constructed from first principles, and only a few physically interpretable parameters need to be estimated from data (see *e.g.* Bard (1974), Varah (1982) or Biegler et al. (1986) for some classical examples). Most commonly, one deals instead with empirical processes for which no functional form of the vector field is available. Early solutions to this (harder) instance of the problem mainly relied on gradient matching (De Hoon et al., 2002; Äijö & Lähdesmäki, 2009). More recently, researchers have leveraged either sensitivity methods, to approximate the unknown vector field with Gaussian processes (Heinonen et al., 2018), or symbolic regression methods to infer it in symbolic form. We refer the reader to La Cava et al. (2021) and Makke & Chawla (2024) for contemporary reviews of the latter case.

In practice, however, one does not need to explicitly infer the vector field in order to impute the missing data, and *we shall take this perspective in the present work*. Prominent examples are the GRU-D (Che et al., 2018) and BRITS (Cao et al., 2018) variants, that model the dynamics underlying the data in some latent, high-dimensional space via linear ODEs; or neural ODEs (Chen et al., 2018) that learn latent albeit nonlinear ODEs. The latter has in fact been modified to suit very different imputation scenarios (Rubanova et al., 2019; Yildiz et al., 2019; Norcliffe et al., 2021; Seifner & Sanchez, 2023). Other works depart from ODEs and assume the dynamics are stochastic. Examples thereof include GP-VAE (Fortuin et al., 2020) and BayOTIDE (Fang et al., 2024b), which leverage Gaussian processes to represent the time evolution, and CSDI (Tashiro et al., 2021) that instead utilizes conditional score-based diffusion models. Finally, researcher have also dispensed with continuous-time models altogether and deployed self-attention mechanisms to impute missing data (Du et al., 2023). Wang et al. (2024) provides a recent and comprehensive review on these and many other imputation methods, and we refer the reader to it for completeness.

Regardless of whether they rely on ODEs or not, all the models above find themselves under the umbrella of the classical paradigm, insofar as they are all optimized with respect to a single empirical process. There are, nevertheless, two recent exceptions. Similar to us, Becker et al. (2023) and d’Ascoli et al. (2024) generate large datasets of ODE systems and their (noisy) observations. Opposite to us, they attempt to explicitly infer the vector fields, and do so in symbolic form. The work of Becker et al. (2023) is however limited to one dimensional ODEs, whereas that of d’Ascoli et al. (2024) is limited to six-dimensional ones. To the best of our knowledge, we present *the first zero-shot solution that is applicable to real-world empirical processes of any dimensionality*.

3 FOUNDATION INFERENCE MODELS FOR DYNAMICAL SYSTEMS

In this section, we introduce a novel methodology for *zero-shot imputation* of missing time series data. Let the series $\mathbf{y}^*(\tau_1), \dots, \mathbf{y}^*(\tau_l)$ correspond to a sequence of l observations on some D -dimensional empirical process $\mathbf{y}^*(t)$, where each observation is represented by a vector $\mathbf{y}^*(\tau_j) \in \mathbb{R}^D$, with $j = 1, \dots, l$. Suppose that some of the components of these observation vectors are missing, and the goal is to impute them back. Our proposal frames the problem of estimating these missing values as an inference task, in which one seeks to infer the ODE solution $\mathbf{x}(t)$ that best *interpolates* the series $\mathbf{y}^*(\tau_1), \dots, \mathbf{y}^*(\tau_l)$, *and thus imputes its missing values*.

The classical formulation of the imputation problem typically involves different missing patterns and in this work we focus on two of them. The first one is the so-called *point-wise missing pattern*, where individual vectors in the series randomly lack some of their components. The second one is the *temporal missing pattern*, where certain components of the vectors in the series are missing over consecutive observation times. To handle them, we make the following two simple assumptions.

First, we assume that for every time series of observations *featuring point-wise missing patterns*, one can always find a certain time scale τ_{simple} , or some (sequential) subset of observations, for which the best interpolating ODE solution is “simple”². Furthermore, we assume that the set of all such simple parametric functions can be well-represented by a heuristically constructed synthetic distribution. Second, we assume that time series *featuring temporal missing patterns* involve more complex interpolating functions, meaning that no such τ_{simple} is to be found in this case. Although more complex in nature, we assume that these functions are *locally* “simple”, and that they often exhibit generic secular and seasonal structures, which encode important information about the missing values and can be well-represented by a second, synthetic distribution over parametric functions. Should these two general assumptions hold true, a model trained to infer both our synthetic set of “simple” parametric functions, and that of functions exhibiting generic, secular and seasonal structures, from noisy and sparse observations on them, will *automatically interpolate any unseen sequence of empirical observations and, consequently, impute all of its missing values*. In the experimental section below, we empirically demonstrate that this is indeed the case in a variety of scenarios.

Our methodology thus consists of two components. The first comprises a synthetic data generation model, and encodes our beliefs about both the “simple” ODE solutions that interpolate the data locally, and the more complex ones that feature global, generic structures. The second corresponds to a neural recognition model of minimal inductive biases, that maps sets of noisy observations onto the space of parametric functions. In what follows, we delve into the details of these two components and name our recognition model as Foundation Inference Model (FIM) for dynamical systems. Figure 1 illustrates the FIM framework.

3.1 SYNTHETIC DATA GENERATION MODEL

In this subsection, we describe the synthetic data generation model we use to sample a large and varied set of ODE solutions, together with their noisy and sparse observations. Given that every ODE solution is a parametric function of time, and that each component of any such D -dimensional function is itself a one-dimensional, parametric function of time, *we focus only on the space of 1D time series*. In other words, we opt for a channel independent strategy (Nie et al., 2023; Han et al., 2024). Let us then define the probability of observing the 1D noisy time series y_1, y_2, \dots, y_l at the observation times $0 \leq \tau_1 < \tau_2 < \dots < \tau_l \leq 1$ — which might correspond to the values taken by any of the components of some D -dimensional process — as

$$\prod_{i=1}^l p_{\text{noise}}(y_i | x_i, \sigma) p(\sigma) \delta \left(x_i - x_0 - \int_0^{\tau_i} f(s) ds \right) p_{\text{grid}}(\tau_1, \dots, \tau_l, \eta_g) p(f, \eta_f) p(x_0), \quad (2)$$

where $\delta(\cdot)$ represents the Dirac delta function, which identifies the ODE solution $x(t)$, evaluated at time τ_i , with $x_0 + \int_0^{\tau_i} f(s) ds$. That is, we understand our ODE solutions as being determined by some initial condition x_0 and the parametric function $f(t)$, which represents the time derivative of $x(t)$. Note that we use the notation x_i to denote $x(\tau_i)$, and that we denote both random variables and their values with the same symbol. Let us now specify each term in Eq. 2, starting from the right.

DISTRIBUTION OVER INITIAL CONDITIONS. We define the prior $p(x_0)$ over initial conditions as a standard Gaussian distribution. A standard Gaussian suffices, because *the values* of every time series we process are first normalized to lie on the unit interval (see Section 3.2.1).

DISTRIBUTION OVER PARAMETRIC FUNCTIONS OF TIME. The prior distribution $p(f, \eta_f)$ factorizes as $p(f | \eta_f) p(\eta_f)$, with $p(\eta_f)$ the prior over the hyperparameter set η_f . The conditional distribution $p(f | \eta_f)$ is a distribution over the space of parametric functions of time, *defined on the unit interval*. It encodes our beliefs about the class of interpolating functions we expect to find in practice. Indeed, as we briefly motivated earlier, we design two such distributions. One represents “simple” parametric functions that are assumed to be typical interpolating functions imputing point-wise missing patterns at the characteristic time scale τ_{simple} . The other represents functions that are locally simple, but that exhibit secular and seasonal structures at longer time scales (*i.e.* $\tau \gg \tau_{\text{simple}}$). Structures that, in turn, are assumed to carry crucial information about temporal missing patterns.

²By simple we loosely mean functions that can be approximated by low-degree polynomials, and functions whose Fourier transform has support at low frequencies only.

We define these distributions by means of random Chebyshev expansions and Gaussian processes with different kernels, and refer the reader to Appendix A.1 for details.

DISTRIBUTION OVER OBSERVATION TIMES. We define the prior distribution $p_{\text{grid}}(\tau_1, \dots, \tau_l, \eta_g)$, with hyperparameter set η_g , to represent missing data patterns that we expect to be relevant in real-world imputation tasks. Again, we consider two such distributions. The first one represents point-wise missing patterns and allows for regular and irregular observation grid instances with different observation count. The second one represents temporal missing patterns and combines point-wise patterns with randomly located observation gaps. We allow the latter to be as large as one-third of the unit interval. Appendix A.2 provides details regarding our implementations.

DISTRIBUTION OVER NOISE PROCESSES. When recording any empirical process, one typically only has access to the mean square error of those measurements. According to the maximum entropy principle, a Gaussian distribution is the best guess one can make about the noise distribution — actually, it is the most likely distribution — given the available information (that is, given those first two moments) (Jaynes, 2003). We choose our noise model $p_{\text{noise}}(y_i|x_i, \sigma)$ accordingly, and set $p(\sigma)$ to also be a Gaussian distribution of zero mean and variance 10^{-1} .

We use the generative model, Eq. 2 above, to sample a large and varied set of noisy and sparse ODE solutions. We refer the reader to Appendix A.4 for details on the specifics of the sampling procedure.

3.2 FOUNDATION INFERENCE MODEL

In this subsection, we introduce a recognition model that exploits ideas from neural operators (Lu et al., 2021; Kovachki et al., 2023) to map time series data onto parametric functions. Indeed, given a set of noisy observations $(y_1, \tau_1), \dots, (y_l, \tau_l)$ on some ODE solution $x(t)$ — sampled from the data generation model, Eq. 2 above — our goal is to infer both the 1D parametric function $f(t)$ and initial condition x_0 that specified $x(t)$ in the first place. In other words, we want to reverse the data generation process. Below, we first introduce a neural interpolation model that is trained to infer the distribution $p(f|\eta_f)$ over “simple” functions, from time series exhibiting point-wise missing patterns. Note that in this setting τ_{simple} is, by construction, of order one. Later, we introduce a second interpolation model that is trained to infer $p(f|\eta_f)$ over functions that are locally “simple” but display global structures at time scales $\tau \gg \tau_{\text{simple}}$, from time series characterized by temporal missing patterns. In what follows, we denote the first interpolation model with FIM- ℓ , for it handles *local* dynamic features, and use FIM to refer to the the second one.

3.2.1 FIM FOR INTERPOLATING POINT-WISE MISSING PATTERNS

In order to interpolate time series featuring point-wise missing patterns, and values of every scale, we first need to normalize every input sequence and rescale their target parametric functions accordingly (see Appendix B.1 for details). Let us label the set of normalized, noisy observations with \mathcal{Y} , the space of rescaled 1D parametric functions with \mathcal{F} and that of rescaled initial conditions with \mathcal{X}_0 . Our interpolation problem can then be understood as the problem of mapping \mathcal{Y} onto both \mathcal{F} and \mathcal{X}_0 . We begin with the first of these two maps.

Let us use ϕ^θ and ψ^θ to denote feedforward (FFN) and sequence processing neural networks, respectively. Let us also denote the trainable network parameters with θ . We now define the function

$$\mathbf{h}^\theta(t) = \phi_3^\theta(\mathbf{u}^\theta, \phi_1^\theta(t)), \quad \text{with } \mathbf{u}^\theta = \phi_2^\theta(\psi_1^\theta(y_1, \tau_1, \dots, y_l, \tau_l)), \quad (3)$$

where ϕ_1^θ and the composition $\phi_2^\theta \circ \psi_1^\theta$ can be interpreted as the trunk and branch nets of DeepONets (Lu et al., 2021), while \mathbf{u}^θ is a representation encoding what we shall call the *context points* of FIM- ℓ . Given the vector-valued, parametric function \mathbf{h}^θ , we now define the mean and variance of a Gaussian distribution *over the values* that the estimated time derivative can take as

$$\hat{f}(t) = \phi_4^\theta(\mathbf{h}^\theta(t)), \quad \log \text{Var}(\hat{f})(t) = \phi_5^\theta(\mathbf{h}^\theta(t)), \quad (4)$$

where, similar to the works of Lakshminarayanan et al. (2017) and Valdenegro-Toro & Mori (2022), the variance $\text{Var}(\hat{f})$ is used to represent the *model’s uncertainty in the estimation of $f(t)$* (see e.g. Figure 3 for an illustration). Next, to perform the map between \mathcal{Y} and \mathcal{X}_0 , we model the initial condition $\hat{x}(0)$ as a Gaussian random variable, whose mean and variance are given by

$$\hat{x}_0 = \phi_6^\theta(\mathbf{u}^\theta), \quad \log \text{Var}(\hat{x}_0) = \phi_7^\theta(\mathbf{u}^\theta). \quad (5)$$

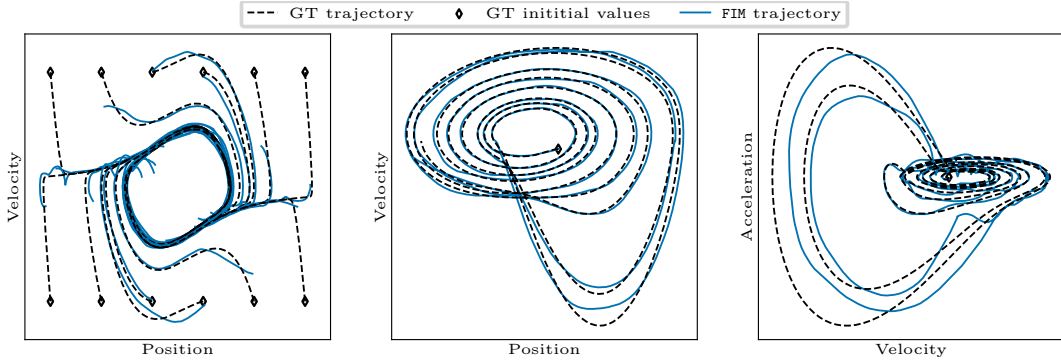


Figure 2: Zero-shot phase portrait reconstruction of two dynamical systems. *Left*: Van der Pol oscillator. *Center and Right*: Rössler attractor in the position-velocity and velocity-acceleration planes, respectively.

Equations 4 and 5 allow us to express the function interpolating the time series $(y_1, \tau_1), \dots, (y_l, \tau_l)$ — at any desired time $\tau \in (0, 1)$ — as $\hat{x}_0 + \int_0^\tau \hat{f}(s) ds$. We train FIM- ℓ in a supervised fashion, to maximize the log-likelihood of Eqs. 4 and 5, and minimize the one-step reconstruction error of the integrated solution, both with respect to the distribution over “simple” functions. We refer the reader to Appendices B.2 and B.3 for details regarding the model architecture and training objective.

PROCESSING DATA OF ANY LENGTH AND DIMENSIONALITY WITH FIM- ℓ . Let us briefly comment on how to use our (pretrained) FIM- ℓ to process time series of any length and dimensionality. We provide further details (and limitations) of our strategies’ implementation in Appendix B.6.

During training, FIM- ℓ processes only 1D time series with at least L_{\min} and at most L_{\max} observations (see Appendix A.2). We define L_{\min} as the minimum number of *context points* FIM generally needs to function, as shorter time series are considered *out-of-distribution*. Similarly, time series with more than L_{\max} observations also fall outside the distribution, not just because of their length, but because their (hidden) interpolating function may not be well-represented by our distribution of “simple” functions. To address this limitation, we first split any target time series longer³ than L_{\max} into successive and overlapping time windows, ensuring that both their *observation count and dynamic features remain within distribution*. That is, we assume that each time window spans a time scale of order $\mathcal{O}(\tau_{\text{simple}})$. Then, we combine the local FIM- ℓ estimates obtained from each window into a global one for the entire target time series (see Appendix B.6). In an analogous manner, we adopt a channel independent strategy and process each component of any target, D -dimensional process independently with FIM- ℓ .

We empirically demonstrate the efficacy of these approaches in Section 4 below.

3.2.2 FIM FOR INTERPOLATING TEMPORAL MISSING PATTERNS

In this subsection, we tackle the interpolation of time series displaying temporal missing patterns by decoupling trends and seasonality from local fluctuations. Suppose we are given a noisy time series with l observations, whose values and observation times lie within the unit interval. Suppose that this time series has been split into K sequential (*i.e.* ordered) sets

$$y_1, \dots, y_{w_1} \cup y_{w_1+1}, \dots, y_{w_1+w_2} \cup \dots \cup y_{l-w_l+1}, \dots, y_l, \quad (6)$$

where w_k is the number of observations within the k th set. Suppose now that the q th set is missing, and the goal is to impute it back.

We assume that *locally*, within every set (even the missing one), the functions underlying the data are well represented by our synthetic distribution of simple functions. That is, we assume that each set spans a time scale of the order $\mathcal{O}(\tau_{\text{simple}})$ and thus, that its underlying function can be modelled well with our *pretrained* FIM- ℓ . We also assume that beyond those time scales ($\tau \geq \tau_{\text{simple}}$), there

³Note that this approach can also be applied to time series of length shorter than L_{\max} , but whose dynamic features are believed to be out-of-distribution.

Table 1: MAE of the inferred time derivative $\dot{\mathbf{x}}(t)$ and ODE solution $\mathbf{x}(t)$ on ODEBench. The standard deviation is calculated across 10 samplings of the corruption schemes.

Model	Inferred time derivative $\dot{\mathbf{x}}(t)$		Reconstructed ODE solution $\mathbf{x}(t)$	
	$\gamma = 0$	$\gamma = 0.05$	$\gamma = 0$	$\gamma = 0.05$
ODEFormer	8.00 \pm 0.40	7.90 \pm 0.60	1.18 \pm 0.05	1.16 \pm 0.05
FIM- ℓ	2.44 \pm 0.05	3.79 \pm 0.05	0.17 \pm 0.01	0.34 \pm 0.01

exist *inter-set*, *global* structures and correlations that carry information about the missing (*i.e.* q th) set. Our task is to define a model that encodes precisely this information. In other words, we require a model that extends the context of FIM- ℓ to longer time scales.

Since FIM- ℓ is trained to deal with normalized data, we first normalize each of the available sets, and denote with s_j the statistics containing information about the local scale (*i.e.* the norms) of the j th set (see Appendix C for details). Let us now process each (normalized and available) set with our *pretrained* encoding network ψ_1^θ , to obtain the sequence

$$(\mathbf{u}_1^\theta, s_1), \dots, (\mathbf{u}_{q-1}^\theta, s_{q-1}), (\mathbf{u}_{q+1}^\theta, s_{q+1}), \dots, (\mathbf{u}_K^\theta, s_K) \text{ with } \mathbf{u}_j^\theta = \phi_2^\theta(\psi_1^\theta(y_1, \tau_1, \dots, y_{w_j}, \tau_{w_j})),$$

where, for simplicity, we relabelled the sub-indices (of the j th set) on the right hand side as $m \leftarrow \sum_{i=1}^{j-1} w_i + m$, with m an integer between 1 and w_j . Our second interpolation model FIM consists of a second sequence processing network ψ_2^φ , with trainable parameter set φ , that computes a representation

$$\mathbf{u}_q^\varphi = \psi_2^\varphi((\mathbf{u}_1^\theta, s_1), \dots, (\mathbf{u}_{q-1}^\theta, s_{q-1}), (\mathbf{u}_{q+1}^\theta, s_{q+1}), \dots, (\mathbf{u}_K^\theta, s_K)), \quad (7)$$

for the missing (*i.e.* q th) set. At this point, we can use the *pretrained* $\phi_1^\theta, \phi_3^\theta, \phi_4^\theta$ and ϕ_5^θ networks of FIM- ℓ to estimate the function $f(t)$ and its variance *along the gap*. That is

$$\hat{f}(t) = \phi_4^\theta(\mathbf{h}^\varphi(t)), \log \text{Var}(\hat{f})(t) = \phi_5^\theta(\mathbf{h}^\varphi(t)), \text{ with } \mathbf{h}^\varphi(t) = \phi_3^\theta(\mathbf{u}_q^\varphi, \phi_1^\theta(t, \theta)). \quad (8)$$

We optimize φ in a supervised manner — *while keeping θ fixed* — to maximize the likelihood of $\hat{f}(t)$ along the missing set, with respect to our synthetic dataset of complex functions that feature global, generic structures and temporal missing patterns. We refer the reader to Appendix C, where we provide additional details and discuss about how to integrate $\hat{f}(t)$ to infer $\hat{x}(t)$ along the gap.

4 EXPERIMENTS

In this section, we test our methodology on widely different imputation tasks, which involve datasets of varying complexity, different dimensionalities and noise signals of very varied nature. We use FIM- ℓ and FIM to impute — *in zero-shot mode* — missing data featuring point-wise and temporal missing patterns, respectively. To be precise, we apply our pretrained models directly to the test sets of the target datasets, *without any parameter fine-tuning*. FIM- ℓ was pretrained to infer 2M ODE solutions from time series with (L_{\min}, L_{\max}) set to $(4, 128)$. FIM was pretrained to infer 500K local ODE solutions from time series with observation gaps that amounted to one-third of the data. Additional information regarding model architecture and hyperparameters, training details and ablation studies can all be found in Appendices B and C.

METRICS. Below we evaluate the performance of our models wrt. the mean-absolute error (MAE). In the Appendix, we also report our results wrt. the root-mean-square error (RMSE) and, in some cases, the R^2 coefficient of determination and the mean-relative error (MRE). Formulas for these metrics can be found in Appendix D.

BASELINES. Depending on the task, we compare our findings against the (symbolic) ODEFormer (d’Ascoli et al., 2024) model; the LatentODE (Chen et al., 2018), NeuralODEProcesses (Norcliffe et al., 2021) and BRITS (Cao et al., 2018) models; the GP-VAE (Fortuin et al., 2020) and the score-based CSDI (Tashiro et al., 2021) models; the (self-attention) SAITS (Du et al., 2023) model; and the (Gaussian process) nPODE (Heinonen et al., 2018) model, among others.

Besides ODEFormer, *all other baselines are trained on their target datasets*.

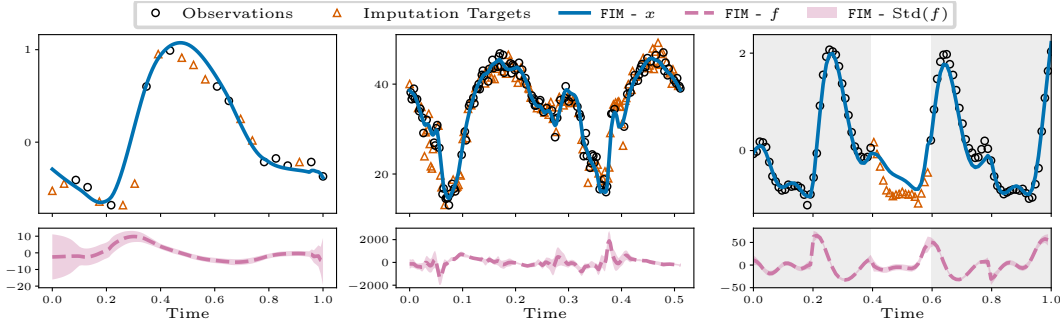


Figure 3: Zero-shot imputation with FIM. *Left and Center*: Point-wise missing imputation in (one dimension of) the *Beijing* and *GuangZhou* datasets, respectively. *(Right)*: Temporal missing imputation in single PCA dimension of the *Motion Capture* dataset.

4.1 PHASE PORTRAIT RECONSTRUCTION

Before testing our methodology in real-world imputation scenarios proper, we explore its ability to accurately reconstruct the phase portrait of complex dynamical systems, using noisy and sparse observations on only one of their coordinates.

Phase portraits are geometric representations of the trajectories of dynamical systems in phase space. They help unveil attractor sets or limit circles and allow to determine, inter alia, how chaotic the systems in question might be (Benettin et al., 1976). In the seminal paper by Packard et al. (1980), the authors demonstrated that one can obtain a faithful phase-portrait representation of any D -dimensional dynamical system, through one of its coordinates, say $x_1(t)$, and all its time derivatives ($\dot{x}_1(t), \ddot{x}_1(t), \dots$) up to order $D - 1$. Carrying out such a reconstruction from noisy and sparse observations on $x_1(t)$ alone, not only entails interpolating the data, but also numerically computing the time derivatives of the interpolating function. In this section, we empirically demonstrate that one can use the hierarchical structure underlying FIM — which treats the time derivatives $\dot{x}_1(t)$ ($f(t)$ in our notation) as a latent variable — to reconstruct, in a zero-shot fashion, the phase portrait of complex dynamical systems.

Suppose we simulate a dynamical system to obtain the solution $\mathbf{x}(t)$ over the interval $[0, T]$, represented on a fine-grid of L points. We then introduce two types of data corruption. The first is multiplicative noise $y_{ij} = (1 + \epsilon)x_{ij}$, with $\epsilon \sim \mathcal{N}(0, \gamma)$, where $i = 1 \dots D$ and $j = 1 \dots L$. The second is random subsampling, where a fraction ρ of the fine-grid is removed (and thus corresponds to a point-wise missing data pattern). For concreteness, we set $T = 10$ and $\gamma = 0.05$. The task is to reconstruct the phase portrait of the dynamical system from the time series y_{11}, \dots, y_{1L} alone.

Let us start with the (nonlinear) Van der Pol oscillator, whose dynamics are given by the second-order ODE $\ddot{x}_1 + \mu(x_1^2 - 1)\dot{x}_1 + x_1 = 0$. This system features a limit circle around $|x_1| = 1$, which gets distorted as one increases the strength of the nonlinear term μ . We set $\mu = 0.5$, simulate the system with 12 different initial conditions and record only the noisy position of the oscillator 128 times per trajectory. The left panel of Figure 2 shows the 12 trajectories inferred by FIM- ℓ on (\dot{x}_1, x_1) phase space, together with the ground-truth, on a *plotting grid* of 2048 points, which amounts to an imputation of 1920 missing points. The agreement is good and the visible deviations are due to small discrepancies in the estimation of the oscillator’s velocity, for some initial conditions. We suspect that such rapidly changing functions are not well-represented by our synthetic distribution of “simple” functions. Next we consider the Rössler system, which is a 3D dynamical system that features a chaotic attractor, and record up to 2048 noisy observations on $x_1(t)$ in order to discern its main features. The center panel of Figure 2 displays the trajectory inferred by FIM- ℓ in (\dot{x}_1, x_1) space, on a plotting grid of 8192 points, which is in very good agreement with the ground-truth. Similarly, the right panel of the same figure displays the inferred trajectory in (\ddot{x}_1, \dot{x}_1) space, obtained by applying FIM- ℓ twice to the noisy observations on $x_1(t)$. Overall, the agreement is still strong and FIM- ℓ only struggles to fit some very rapid changes in the acceleration function, which definitely lie out-of-distribution. We provide details of these computations and explore the systems further in Appendices E.1 and E.2, respectively.

Table 2: MAE (at missing values) on 8 datasets featuring 50% *point-wise missing patterns*. Baselines scores for *GuangZhou* and *Solar* are extracted from Fang et al. (2024a). The rest are extracted from Du et al. (2024). See Appendix G for standard deviations and additional baselines.

Method	Air quality		GuangZhou	Traffic		Solar	Electricity	
	Beijing	Italy		PeMS	Pedestrian		ETT_h1	Electricity
BRITS	0.169	0.321	3.335	0.287	0.259	1.985	0.238	1.124
SAITS	0.194	0.285	3.391	0.302	0.205	1.827	0.223	1.399
GP-VAE	0.258	0.453	3.419	0.346	0.451	1.810	0.414	1.099
CSDI	0.144	0.958	3.202	0.288	0.351	0.804	0.318	0.798
BayOTIDE	-	-	2.687	-	-	0.734	-	-
FIM- ℓ	0.166	0.215	2.427	0.365	0.273	0.595	0.279	0.083

The discussion above yielded a qualitative picture of the inference capabilities of FIM- ℓ . To obtain a more quantitative perspective, we now compare FIM- ℓ against the ODEFormer model of d’Ascoli et al. (2024). ODEFormer is trained *offline* to infer the vector field $\mathbf{f}(\mathbf{x})$ of dynamical systems in symbolic form. We estimate $\dot{\mathbf{x}}(t)$ with ODEFormer by first solving their inferred ODE, to obtain an estimate of the ODE solution $\mathbf{x}(t)$, and then evaluating their inferred vector field along their estimated $\hat{\mathbf{x}}(t)$. As target dataset we analyse ODEBench, which was also introduced by d’Ascoli et al. (2024). ODEBench consists of 63 autonomous ODEs of different dimensionalities (specifically, 23 1D, 28 2D, 10 3D and 2 4D equations) and their solutions. The latter are represented on a fine-grid of 512 points. We set $\rho = 0.5$ (which defines point-wise missing patterns) and let γ be either 0 or 0.05. We then compute the MAE of ODEFormer and FIM- ℓ on the estimation of both $\dot{\mathbf{x}}(t)$ and $\mathbf{x}(t)$ with respect to the ground-truth trajectories across all 63 target ODEs. Table 1 reports our results averaged over all ODEs and shows that FIM- ℓ outperforms ODEFormer in every case.

Some final remarks are in order. First, d’Ascoli et al. (2024) originally report R^2 accuracies in their paper. We also report these per dimension in Table 9 of Appendix E.3, as well as RMSEs. Our conclusions remain unchanged. Second, these results also reveal that, despite being trained on additive noise only, FIM- ℓ can handle multiplicative noise well. Third, we empirically demonstrate that FIM- ℓ is also superior to LatentODE trained on the iconic Lorenz systems in Appendix E.4. Fourth, we also demonstrate that FIM- ℓ outperforms the very recent NeuralODEProcesses model on low-data regimes in Appendix E.5. All together, these results reflect the capabilities of FIM- ℓ to not only impute point-wise missing data in dynamical systems, but also accurately reconstruct their phase portraits, *both in zero-shot mode*.

4.2 IMPUTATION OF POINT MISSING PATTERNS

In this subsection we evaluate FIM- ℓ on 8 real-world, high-dimensional datasets featuring point-wise missing data. Specifically, we study the *Guangzhou* dataset, which contains traffic speed records with 214 channels and 500 observations, and the *Solar* dataset, which consists of solar-power generation records with 137 channels and 52560 observations. We obtained both the (pre-processed) datasets and the corresponding baseline performance from Fang et al. (2024a). We also study two popular air quality datasets from *Beijing* and *Italy*, which have 132 channels with 1458 observations, and 13 channels with 774 observations, respectively; the *Electricity* and *ETT-h1* datasets of electricity consumption, common in forecasting studies, with 370 (1457) and 7 (358) channels (observations) each; and two additional traffic-related datasets, namely the *PeMS* dataset of road occupancy with 862 channels and 727 observations, and the single-channel *Pedestrian* dataset, which reports pedestrian activity in Australia and consists of 3633 observations. We obtain this second set of 6 (preprocessed) datasets, together with the corresponding baseline performance from Du et al. (2024).

After being split into train, validation and test sets, fifty percent of these subsets is randomly removed, defined as missing and set aside for evaluation. We only make use of the (available 50% of the) test subsets with FIM- ℓ . Figure 3 illustrates the type of *zero-shot* ODE solutions inferred by FIM- ℓ on the *Beijing* and *Guangzhou* datasets (left and center). The bottom panels portrait instead the inferred (time) derivatives of the interpolating functions, together with the confidence of the model, which increases in regions with high, local information. Table 2 reports the average MAE at the missing values for all models. Remarkably, FIM- ℓ outperforms all baselines in 4 out of 8

Table 3: MAE (at missing values) on Motion Capture (MC) and Navier-Stokes datasets featuring *temporal missing patterns* of 20%. The large error bars in the MC dataset have been reported before (Heinonen et al., 2018). (Cubic) spline(F) includes a Savgol filter.

Model	<i>Motion Capture</i>		<i>Navier Stokes</i>	
	PCA	No PCA	PCA	No PCA
LatentODE	1.658 ± 0.989	-	0.076 ± 0.030	-
(Cubic) spline	3.362 ± 1.175	4.209 ± 1.436	0.085 ± 0.003	0.083 ± 0.003
(Cubic) spline(F)	2.897 ± 0.871	2.998 ± 0.881	0.084 ± 0.000	0.075 ± 0.002
FIM	1.765 ± 0.627	1.611 ± 0.453	0.063 ± 0.003	0.051 ± 0.002

datasets, comes second in one, and third in two, which suggests that *there is indeed enough local information to perform the data imputation with “simple” functions in these use cases*. We close this subsection by referring the reader to Appendix F, where we report the scores of additional, albeit less common baselines, as well as our results on the data splits investigated by Du et al. (2023).

4.3 IMPUTATION OF TEMPORAL MISSING PATTERNS

In this subsection, we look into the harder problem of imputing time series data featuring *temporal missing patterns*. Indeed, we explore the problem setup proposed by Heinonen et al. (2018), in which (about) 20% of the data from the middle of the time series is missing completely. More precisely, we consider their human Motion Capture dataset, which consists of 43 trajectories, each with 50 channels and 100 observations. We also apply their setup to the Navier-Stokes simulation of Course & Nair (2023), which instead contains 596602 channels. To be able to handle the (high) dimensionality of the datasets, Heinonen et al. (2018) projects the data to latent space using PCA, and trains their models to perform the imputation there (see Appendix G for details). We follow their methodology and train a LatentODE model, to outperform the results reported by Heinonen et al. (2018). Additionally, we compare against a naive spline⁴ interpolation.

Having set the stage, we leverage our pretrained FIM to infer the ODE solution that best imputes the missing data in PCA space, and report the MAE at the missing values, after projecting back to data space, in Table 3. Since FIM (and spline) can be applied to each channel independently, we also report the MAE we obtain by imputing the data directly in (high-dimensional) data space. Again, FIM performs comparably to (or even better than) LatentODE in the Motion Capture dataset, and outperforms it on the Navier-Stokes case, *despite not being trained on the target data*. Note that imputing the data in high-dimensional space helps avoid the errors introduced by the PCA projections. The right panel of Figure 3 illustrates the class of *zero-shot* ODE solutions inferred by FIM in the Motion Capture dataset, and demonstrates how FIM leverages the global, seasonal structures outside the gap to impute the (locally simpler) missing data. The agreement is strong.

5 CONCLUSIONS

In this work, we introduced a novel methodology for *zero-shot imputation* of time series data, whose underlying dynamics are assumed to be governed by ordinary differential equations (ODEs). We empirically demonstrated that *one and the same* Foundation Inference Model (FIM) can impute datasets of any dimensionality, featuring noise signals of very different nature, even in cases which do not naturally admit a description in terms of ODEs. In fact, we showed that FIM often outperforms SOTA models that are trained to the target distributions.

The main limitation of our methodology is clearly imposed by our synthetic distributions. Evaluating FIM on empirical datasets whose distribution significantly deviates from our synthetic distribution will inevitably yield poor estimates. The left panel of Figure 2 provides such an example. Indeed, for some initial conditions, the velocity of the Van der Pol oscillator features rapid changes that are not well represented in our synthetic distribution of simple functions.

Future work shall extend our decoupling of local and global features of the imputation model to the problem of *zero-shot forecasting*.

⁴<https://scipy.org/>

6 REPRODUCIBILITY STATEMENT

The Appendix includes all information required to reproduce our presented methods and results. Let us therefore provide a short overview of its contents, focused on the parts related to reproducibility.

An important part of our methodology is our *synthetically generated training dataset*, which Appendix A is dedicated to. The generation and hyperparameter choices are described extensively in Appendix A.1 (distributions over functions), Appendix A.2 (observation grids) and Appendix A.3 (noise processes). Appendix A.4 schematizes the whole generation algorithm.

Appendix B includes all details related to $\text{FIM-}\ell$, our model for *point-wise missing pattern imputation*. In particular, Appendix B.2 describes the complete model architecture, including hyperparameters of our single trained $\text{FIM-}\ell$ model, and model inputs and outputs. Its training procedure is discussed in Appendix B.4, including hyperparameters for the optimizer and computing resources, whereas Appendix B.3 states the training objective.

The details for FIM, our model for *temporal missing pattern imputation*, are given in Appendix C. Appendix C.2 describes the complete model architecture, where we also include the hyperparameters used for our single trained FIM model. The training details are given in Appendix C.4, including hyperparameters of the optimizer and computing resources, and Appendix C.3 states the associated training objective.

Equations of the *evaluation metrics* used for comparisons in our experiments, and remarks about their usage in the different applications, are provided in Appendix D. Training details and computing resources for *LatentODE*, one of our baselines, are stated (for each dataset individually) in Appendices E.4.2, G.1.2 and G.2.2.

The *datasets in our experiments* are addressed individually in their own subsection in Appendices E, F and G. Each subsection contains either generation hyperparameters or links to their sources, and the applied pre-processing steps.

Finally, we provide an *anonymized link* to the *source code and weights* of our trained $\text{FIM-}\ell$ model in the supplementary material of this submission, including a script to regenerate Figure 6 for the ODEBench dataset.

ACKNOWLEDGEMENTS

This research has been funded by the Federal Ministry of Education and Research of Germany and the state of North-Rhine Westphalia as part of the Lamarr-Institute for Machine Learning and Artificial Intelligence.

REFERENCES

- Tarmo Äijö and Harri Lähdesmäki. Learning gene regulatory networks from gene expression measurements using non-parametric molecular kinetics. *Bioinformatics*, 25(22):2937–2944, 2009.
- Yonathan Bard. *Nonlinear parameter estimation*. Academic Press, New York, 1974.
- Sören Becker, Michal Klein, Alexander Neitz, Giambattista Parascandolo, and Niki Kilbertus. Predicting ordinary differential equations with transformers. In *International Conference on Machine Learning*, pp. 1978–2002. PMLR, 2023.
- Giancarlo Benettin, Luigi Galgani, and Jean-Marie Strelcyn. Kolmogorov entropy and numerical experiments. *Physical Review A*, 14(6):2338, 1976.
- Johann Bernoulli. *Extrait de la Réponse de M. Bernoulli à M. Herman, datée de Basle le 7. Octobre 1710*. Mémoires de l’Ac. Royale des Sciences, Boudot, Paris, 1710, 1712.
- L. T. Biegler, J. J. Damiano, and G. E. Blau. Nonlinear parameter estimation: A case study comparison. *AIChE Journal*, 32(1):29–45, 1986. doi: <https://doi.org/10.1002/aic.690320105>.

- Rishi Bommasani, Drew A Hudson, Ehsan Adeli, Russ Altman, Simran Arora, Sydney von Arx, Michael S Bernstein, Jeannette Bohg, Antoine Bosselut, Emma Brunskill, et al. On the opportunities and risks of foundation models. *arXiv preprint arXiv:2108.07258*, 2021.
- Wei Cao, Dong Wang, Jian Li, Hao Zhou, Lei Li, and Yitan Li. Brits: Bidirectional recurrent imputation for time series. *Advances in neural information processing systems*, 31, 2018.
- Stephanie Chan, Adam Santoro, Andrew Lampinen, Jane Wang, Aaditya Singh, Pierre Richemond, James McClelland, and Felix Hill. Data distributional properties drive emergent in-context learning in transformers. *Advances in Neural Information Processing Systems*, 35:18878–18891, 2022.
- Zhengping Che, Sanjay Purushotham, Kyunghyun Cho, David Sontag, and Yan Liu. Recurrent neural networks for multivariate time series with missing values. *Scientific reports*, 8(1):6085, 2018.
- Ricky TQ Chen, Yulia Rubanova, Jesse Bettencourt, and David K Duvenaud. Neural ordinary differential equations. *Advances in neural information processing systems*, 31, 2018.
- Kevin Course and Prasanth B Nair. State estimation of a physical system with unknown governing equations. *Nature*, 622(7982):261–267, 2023.
- Stéphane d’Ascoli, Sören Becker, Philippe Schwallier, Alexander Mathis, and Niki Kilbertus. ODEFormer: Symbolic regression of dynamical systems with transformers. In *The Twelfth International Conference on Learning Representations*, 2024.
- Michiel JL De Hoon, Seiya Imoto, Kazuo Kobayashi, Naotake Ogasawara, and Satoru Miyano. Inferring gene regulatory networks from time-ordered gene expression data of bacillus subtilis using differential equations. In *Biocomputing 2003*, pp. 17–28. World Scientific, 2002.
- Wenjie Du, David Côté, and Yan Liu. Saits: Self-attention-based imputation for time series. *Expert Systems with Applications*, 219:119619, 2023.
- Wenjie Du, Jun Wang, Linglong Qian, Yiyuan Yang, Fanxing Liu, Zepu Wang, Zina Ibrahim, Haoxin Liu, Zhiyuan Zhao, Yingjie Zhou, Wenjia Wang, Kaize Ding, Yuxuan Liang, B. Aditya Prakash, and Qingsong Wen. Tsi-bench: Benchmarking time series imputation. *arXiv preprint arXiv:2406.12747*, 2024.
- Emilien Dupont, Arnaud Doucet, and Yee Whye Teh. Augmented neural odes. *Advances in neural information processing systems*, 32, 2019.
- Shikai Fang, Qingsong Wen, Yingtao Luo, Shandian Zhe, and Liang Sun. Bayotide: Bayesian online multivariate time series imputation with functional decomposition, 2024a.
- Shikai Fang, Qingsong Wen, Yingtao Luo, Shandian Zhe, and Liang Sun. BayOTIDE: Bayesian online multivariate time series imputation with functional decomposition. In *Proceedings of the 41st International Conference on Machine Learning*, volume 235, pp. 12993–13009. PMLR, 2024b.
- Vincent Fortuin, Dmitry Baranchuk, Gunnar Rätsch, and Stephan Mandt. Gp-vae: Deep probabilistic multivariate time series imputation. In *Proc. AISTATS*, pp. 1651–1661, 2020.
- Lu Han, Han-Jia Ye, and De-Chuan Zhan. The capacity and robustness trade-off: Revisiting the channel independent strategy for multivariate time series forecasting. *IEEE Transactions on Knowledge and Data Engineering*, 2024.
- Markus Heinonen, Cagatay Yildiz, Henrik Mannerström, Jukka Intosalmi, and Harri Lähdesmäki. Learning unknown ode models with gaussian processes. In *International conference on machine learning*, pp. 1959–1968. PMLR, 2018.
- Jacobus Henricus van ’t Hoff. *Studies in Chemical Dynamics*. Amsterdam: F. Mueller and Co. London: Williams and Norgate, 1986.
- Edwin Thompson Jaynes. *Probability Theory: the Logic of Science*. Cambridge University Press, 2003.

- Günter Klambauer, Thomas Unterthiner, Andreas Mayr, and Sepp Hochreiter. Self-normalizing neural networks. *Advances in neural information processing systems*, 30, 2017.
- Nikola Kovachki, Zongyi Li, Burigede Liu, Kamyar Aizzadenesheli, Kaushik Bhattacharya, Andrew Stuart, and Anima Anandkumar. Neural operator: Learning maps between function spaces with applications to pdes. *Journal of Machine Learning Research*, 24(89):1–97, 2023.
- William La Cava, Patryk Orzechowski, Bogdan Burlacu, Fabrício Olivetti de França, Marco Virgolin, Ying Jin, Michael Kommenda, and Jason H Moore. Contemporary symbolic regression methods and their relative performance. *arXiv preprint arXiv:2107.14351*, 2021.
- Balaji Lakshminarayanan, Alexander Pritzel, and Charles Blundell. Simple and scalable predictive uncertainty estimation using deep ensembles. *Advances in neural information processing systems*, 30, 2017.
- Hugo Larochelle, Dumitru Erhan, and Yoshua Bengio. Zero-data learning of new tasks. In *AAAI*, volume 1, pp. 3, 2008.
- Edward N Lorenz. Deterministic nonperiodic flow. *Journal of atmospheric sciences*, 20(2):130–141, 1963.
- Ilya Loshchilov and Frank Hutter. Sgdr: Stochastic gradient descent with warm restarts. *arXiv preprint arXiv:1608.03983*, 2016.
- Ilya Loshchilov and Frank Hutter. Decoupled weight decay regularization. *arXiv preprint arXiv:1711.05101*, 2017.
- Alfred James Lotka. *Elements of physical biology*. Williams & Wilkins, 1925.
- Lu Lu, Pengzhan Jin, Guofei Pang, Zhongqiang Zhang, and George Em Karniadakis. Learning nonlinear operators via deeponet based on the universal approximation theorem of operators. *Nature machine intelligence*, 3(3):218–229, 2021.
- Nour Makke and Sanjay Chawla. Interpretable scientific discovery with symbolic regression: a review. *Artificial Intelligence Review*, 57(1):2, 2024.
- Isaac Newton. *Philosophiæ Naturalis Principia Mathematica*. cf. especially Liber de Motu I Sects. II, III, VII. London, 1687.
- Yuqi Nie, Nam H Nguyen, Phanwadee Sinthong, and Jayant Kalagnanam. A time series is worth 64 words: Long-term forecasting with transformers. In *The Eleventh International Conference on Learning Representations*, 2023. URL <https://openreview.net/forum?id=Jbdc0vTOcol>.
- Bernd R Noack, Konstantin Afanasiev, Marek Morzyński, Gilead Tadmor, and Frank Thiele. A hierarchy of low-dimensional models for the transient and post-transient cylinder wake. *Journal of Fluid Mechanics*, 497:335–363, 2003.
- Alexander Norcliffe, Cristian Bodnar, Ben Day, Jacob Moss, and Pietro Liò. Neural {ode} processes. In *International Conference on Learning Representations*, 2021. URL <https://openreview.net/forum?id=27acGyyI1BY>.
- Norman H Packard, James P Crutchfield, J Doyne Farmer, and Robert S Shaw. Geometry from a time series. *Physical review letters*, 45(9):712, 1980.
- Brooks Paige and Frank Wood. Inference networks for sequential monte carlo in graphical models. In *International Conference on Machine Learning*, pp. 3040–3049. PMLR, 2016.
- Yulia Rubanova, Tian Qi Chen, and David Duvenaud. Latent Ordinary Differential Equations for Irregularly-Sampled Time Series. In *Advances in Neural Information Processing Systems 32*, pp. 5321–5331, 2019.
- Abraham Savitzky and Marcel JE Golay. Smoothing and differentiation of data by simplified least squares procedures. *Analytical chemistry*, 36(8):1627–1639, 1964.

- Patrick Seifner and Ramses J Sanchez. Neural Markov jump processes. In *Proceedings of the 40th International Conference on Machine Learning*, volume 202. PMLR, 2023.
- Satya Narayan Shukla and Benjamin Marlin. Multi-time attention networks for irregularly sampled time series. In *ICML Workshop on the Art of Learning with Missing Values (Artemiss)*, 2020.
- Andreas Stuhlmüller, Jacob Taylor, and Noah Goodman. Learning stochastic inverses. *Advances in neural information processing systems*, 26, 2013.
- Yusuke Tashiro, Jiaming Song, Yang Song, and Stefano Ermon. CSDI: Conditional score-based diffusion models for probabilistic time series imputation. *Advances in Neural Information Processing Systems*, 34:24804–24816, 2021.
- Matias Valdenegro-Toro and Daniel Saromo Mori. A deeper look into aleatoric and epistemic uncertainty disentanglement. In *2022 IEEE/CVF Conference on Computer Vision and Pattern Recognition Workshops (CVPRW)*, pp. 1508–1516. IEEE, 2022.
- James M Varah. A spline least squares method for numerical parameter estimation in differential equations. *SIAM Journal on Scientific and Statistical Computing*, 3(1):28–46, 1982.
- Jean-Philippe Vert, Koji Tsuda, and Bernhard Schölkopf. A primer on kernel methods. *Kernel methods in computational biology*, 47:35–70, 2004.
- Vito Volterra. *Variazioni e fluttuazioni del numero d'individui in specie animali conviventi*, volume 2. Società anonima tipografica" Leonardo da Vinci", 1927.
- Jack M Wang, David J Fleet, and Aaron Hertzmann. Gaussian process dynamical models for human motion. *IEEE transactions on pattern analysis and machine intelligence*, 30(2):283–298, 2007.
- Jun Wang, Wenjie Du, Wei Cao, Keli Zhang, Wenjia Wang, Yuxuan Liang, and Qingsong Wen. Deep learning for multivariate time series imputation: A survey. *arXiv preprint arXiv:2402.04059*, 2024.
- Christopher Williams and Carl Rasmussen. Gaussian processes for regression. *Advances in neural information processing systems*, 8, 1995.
- Cagatay Yildiz, Markus Heinonen, and Harri Lahdesmaki. Ode2vae: Deep generative second order odes with bayesian neural networks. *Advances in Neural Information Processing Systems*, 32, 2019.

A SYNTHETIC DATA GENERATION MODEL: SPECIFICS

A.1 ON THE DISTRIBUTION OVER PARAMETRIC FUNCTIONS OF TIME

In this section we define two distributions over the space of parametric functions. We use the first one to train our FIM for interpolation. We use the second one to train our extended FIM for imputation.

A.1.1 DISTRIBUTION OVER “SIMPLE” INTERPOLATION FUNCTIONS

To train our model for *point-wise missing patterns*, we define $p(f|\eta_f)$ either via Gaussian processes (GP) with Radial Basis Function (RBF) kernels (Williams & Rasmussen, 1995; Vert et al., 2004), or as truncated Chebyshev expansions, whose coefficients and degree are both randomly sampled. Each alternative has different η_f hyperparameters.

In the case of RBF kernels, there is a single free hyperparameter, the *lengthscale* η_f , which controls the scale at which variations take place. A small η_f results in parametric functions with short-range fluctuations, whereas larger η_f produce smoother functions that capture broader trends. We define $p(\eta_f)$ as a mixture of two Beta distributions, with equal mixing coefficients. To wit

$$p(\eta_f) = \frac{1}{2}\text{Beta}(\eta_f|2, 10) + \frac{1}{2}\text{Beta}(\eta_f|2, 5). \quad (9)$$

Here, the first component returns functions with faster change (*i.e.* higher frequency), whereas the second component returns smoother functions.

In the case of (the M -order) truncated Chebyshev expansions, we write

$$f(t) = \sum_{m=1}^M a_m T_m(t), \quad (10)$$

where $T_m(t)$ is the m th Chebyshev polynomial with (real) coefficient a_m . Now, in order to generate a random parametric function with Eq. 10, we sample both the degree M and the set of coefficients $\{a_1, \dots, a_M\}$ from the prior $p(\eta_f)$. Intuition says one would like high-order polynomials to occur rarely. It also says one would like the scale of their coefficients to be small (see also the work of *e.g.* Chan et al. (2022)). We therefore (implicitly) define the distribution $p(\eta_f)$ over hyperparameters as

$$(a_1, \dots, a_M) \sim \mathcal{N}\left(0, \frac{1}{M}\right), \text{ with } M \sim \text{Zipf}(2). \quad (11)$$

In practice, we generate a synthetic dataset of $2M$ parametric functions (200K for the test set), each of which is evaluated on a *fine grid* of $L_{max} = 128$ *points*. This fine grid is defined regularly on the unit interval $[0, 1]$. Half of this dataset consists of random Chebyshev expansions. The other half consists of parametric functions sampled via GPs.

A.1.2 DISTRIBUTION OVER IMPUTATION FUNCTIONS WITH GLOBAL PATTERNS

To train our model for *temporal missing patterns*, we require data with *trends* and *seasonality*, such that our model learns to use these (global) patterns to impute the missing data. We hence define $p(f|\eta_f)$ as again via GPs, but opt for Periodic kernels, which exhibit the required *seasonality*.

Periodic kernels are specified by two free hyperparameters: the *lengthscale*, denoted by η_f^l , and the *period*, denoted by η_f^p . The lengthscale determines the local fluctuations of the function, as described in Appendix A.1.1. The period determines the frequency of repetitions of the function, *i.e.* the seasonality.

We sample both hyperparameters independently. In other words, our distribution over Periodic kernel GPs $p(\eta_f)$ factorizes as $p(\eta_f) = p(\eta_f^l, \eta_f^p) = p(\eta_f^l)p(\eta_f^p)$. We define uniform distributions for both hyperparameters:

$$\begin{aligned} p(\eta_f^l) &= \mathcal{U}(\eta_f^l|[0.75, 1]) \\ p(\eta_f^p) &= \mathcal{U}(\eta_f^p|[0.3, 0.5]) \end{aligned}$$

We generate a dataset of 500k parametric functions (50K for the test set). Each function is evaluated on a regular *fine grid* of $L_{\max} = 256$ points on the unit interval $[0, 1]$.

Note that we do not need to explicitly address *trends* in the parametric functions over time. A sample from the defined GPs will (*a.s.*) have a non-zero mean. During data generation (see Appendix A.4), these deviations will accumulate over time, such that the corresponding ODE solutions exhibit trends naturally. In combination with instance normalization during model input processing (see Appendix C.1), this setup covers a variety of trends.

A.2 ON THE DISTRIBUTION OVER OBSERVATION GRIDS

In this section we define two distributions over observation grids. We use the first one to train our FIM for interpolation. We use the second one to train our extended FIM for imputation.

A.2.1 OBSERVATION GRIDS ENCODING POINT-WISE MISSING PATTERNS

We define the prior distribution over observation grids $p_{\text{grid}}(\tau_1, \dots, \tau_l, \eta_g)$ in a way that it allows for both regular and irregular observation grid instances, each with at most L_{\max} and at least L_{\min} observations. Note that the latter number defines the *minimum number of context points needed for FIM to function*.

Let us recall that our parametric functions $f(t)$ are evaluated on a fine grid of 128 points (see Appendix A.1 above) over the unit interval $[0, 1]$. This fine grid is subsequently subsampled randomly, to define the random observation times τ_1, \dots, τ_l . We employ two subsampling schemes — *regular* and *irregular* — which occur with equal probability within our entire dataset.

Regular scheme. In this scheme the observation times are obtained from the fine grid by strides of regular length, where the stride length is sampled from the $\text{Uniform}([1, 2, \dots, 16])$ distribution. Note that this distribution defines $p(\eta_g)$.

Irregular scheme. In this scheme the observation times are instead defined via Bernoulli masks, whose survival probabilities (here denoted by η_g) are sampled from a categorical distribution $p(\eta_g)$. The latter is defined over the set $\{0.0625, 0.25, 0.5\}$ with class probabilities $\{0.5, 0.25, 0.25\}$, respectively.

Note that we ensure that there are at least $L_{\min} = 8$ observations in each time series, by rejecting observation grid instances with less than eight points. In contrast, there are time series with at most $L_{\max} = 128$ observations.

A.2.2 OBSERVATION GRIDS ENCODING TEMPORAL MISSING PATTERNS

To train our model for *temporal missing patterns*, the observation grids of our training data must exhibit such patterns. We sample such grids in a two-step process.

In the *point-wise step*, as for the observation grids sampled in Appendix A.2.1, we only employ point-wise subsampling schemes. These are required for our model can handle irregular grid time series data of variable lengths.

In the *temporal step* we introduce the *temporal missing patterns*, by dropping a consecutive range of observations. We train our model to impute these dropped values.

More formally, let τ_i denote times in the *point-wise* observation grid and $\tilde{\tau}_i$ denote times in the *temporal missing pattern* observation grid. Then their joint distribution depends on two hyperparameters, η_g^{point} and η_g^{temp} , and factorizes as

$$p_{\text{grid}}(\tilde{\tau}_1, \dots, \tilde{\tau}_k, \tau_1, \dots, \tau_l, \eta_g^{\text{temp}}, \eta_g^{\text{point}}) = p_{\text{temp}}(\tilde{\tau}_1, \dots, \tilde{\tau}_k | \tau_1, \dots, \tau_l, \eta_g^{\text{temp}}) p(\eta_g^{\text{temp}}) p_{\text{point}}(\tau_1, \dots, \tau_l | \eta_g^{\text{point}}) p(\eta_g^{\text{point}}).$$

where $\{\tilde{\tau}_i\}_{i=1}^k \subseteq \{\tau_i\}_{i=i}^l$.

Let us now report the specifics for both steps:

Point-wise step. One half of the observation grids are generated with a *regular* subsampling scheme, sampling stride lengths from $\text{Uniform}([1, 2, 3, 4])$. The other half is generated with a *irregular* subsampling scheme, sampling from a Bernoulli distribution with survival probability 0.5.

Temporal step. To generate a missing pattern in the time series, we first sample the position of the missing pattern from a uniform distribution, specifically $\text{Uniform}(1, 3)$, which determines the window that will be masked. The length of the missing pattern is randomly sampled from a uniform distribution in the range $[10, 30]$. The remaining part of the time series is then split into four equal windows.

A.3 ON THE DISTRIBUTION OVER NOISE PROCESSES

Let $x : \mathbb{R}_+ \rightarrow \mathbb{R}$ be a time-dependent trajectory. We define the distribution over noise processes on observations $x(t) \in \mathbb{R}$ of such trajectory to factorize, such that the noise process is fixed for each trajectory. More formally, denoting the noise process by σ and the noisy trajectory by y , we assume

$$p_{\text{noise}}(y(t), x(t), \sigma(t)) = p_{\text{noise}}(y(t) | x(t), \sigma)p(\sigma) \text{ for all } t \in \mathbb{R}.$$

As outlined in Section 3.1, we use additive Gaussian noise

$$p_{\text{noise}}(y(t) | x(t), \sigma) = \mathcal{N}(x(t), \sigma)$$

for our synthetic datasets. Here, the noise process is defined only by a single value: the standard deviation σ of a Gaussian distribution. Hence, our choice of a distribution over noise processes reduces to a choice of a suitable distribution for σ . We use $p(\sigma) = \mathcal{N}(0, \lambda)$ in our synthetic datasets, interpreting negative samples for σ as their absolute value⁵.

The value of λ differs between our two synthetic datasets. In our dataset for *point-wise missing patterns*, we use $\lambda = 0.1$ and in our dataset for *temporal missing patterns*, we use $\lambda = 0.05$. We reduce λ for the temporal-missing patterns to retain more structure of the trajectory, such that the model can learn to impute based on the structure of the time series.

A.4 ON THE GENERATION OF THE SYNTHETIC DATASET

In this subsection we schematize the data generation process. Underlying this process is a sampling procedure of noisy time series data, based on samples of random functions, observation grids and noise processes. The corresponding distributions are described in Appendices A.1-A.3.

To generate the j th instance of our synthetic datasets, we utilise these distributions in the following generation steps:

1. Sample a *function*

$$f_j \sim p(f | \eta_{f,j}), \quad \text{where } \eta_{f,j} \sim p(\eta_f),$$

and record its values $\{f_j(t_i)\}_{i=1}^L$ on the *fine grid* $\{t_i\}_{i=1}^L$, the regular grid on the unit interval $[0, 1]$.

2. Sample a *initial value* $x_{0j} \sim \mathcal{N}(0, 1)$ that defines the ODE solution

$$x_j(t) = x_{0j} + \int_0^t f_j(s) ds$$

and record its values $\{x_j(t_i)\}_{i=1}^L$ on the *fine grid*.

3. Sample a *observation grid*

$$\tau_{1j}, \dots, \tau_{lj} \sim p_{\text{grid}}(\tau_1, \dots, \tau_l | \eta_{g,j}), \quad \text{where } \eta_{g,j} \sim p(\eta_g),$$

that defines a time series with (clean) observations $\{(x_{ij} = x(\tau_{ij}), \tau_{ij})\}_{i=1}^l$ of the ODE solution.

4. Sample *noisy observations*

$$y_{ij} \sim p_{\text{noise}}(y | x_{ij}, \sigma_j), \quad \text{where } \sigma_j \sim p(\sigma),$$

of the ODE solution that define the time series $\{(y_{ij}, \tau_{ij})\}_{i=1}^l$.

Note that each step consists of i.i.d. samples of their respective (hierarchical) distributions. Thus, each instance of our synthetic datasets is also i.i.d..

⁵This distribution is also called a folded Gaussian distribution.

B FIM FOR LOCAL INTERPOLATION: ADDITIONAL DETAILS

In this section, we begin with instance normalization – in section B.1 – as a pre-processing step for handling times series of varying scales. We then outline the training objective in section B.3, focusing on the loss function design. Next, we discuss methods for processing time series of any length and dimensionality (section B.6).

B.1 INPUT PRE-PROCESSING AND OUTPUT POST-PROCESSING

To accommodate time series of all scales, we employ min-max-normalization for the observation values and times *per time series* before processing them with FIM- ℓ and renormalize the model outputs accordingly. To express this instance normalization in equations, let $(y_1, \tau_1), \dots, (y_l, \tau_l)$ be a set of noisy observations, following the notation of Section 3.2.1 and denote

$$\tau_{\min} = \min_{i=1, \dots, l} \tau_i, \quad \tau_{\max} = \max_{i=1, \dots, l} \tau_i, \quad y_{\min} = \min_{i=1, \dots, l} y_i, \quad y_{\max} = \max_{i=1, \dots, l} y_i \quad . \quad (12)$$

Before applying FIM- ℓ as described in Section 3.2.1, we replace the inputs by their normalized values:

$$y_i \leftarrow \frac{y_i - y_{\min}}{y_{\max} - y_{\min}}, \quad \tau_i \leftarrow \frac{\tau_i - \tau_{\min}}{\tau_{\max} - \tau_{\min}} \quad (13)$$

Let $\hat{f}(t)$, $\log \text{Var}(\hat{f})(t)$, \hat{x}_0 and $\text{Var}(\hat{x}_0)$ be the outputs of FIM- ℓ , following Equations 4 and 5 of Section 3.2.1, given the normalized inputs. Under the renormalization maps

$$y \leftarrow (y_{\max} - y_{\min})y + y_{\min}, \quad t \leftarrow (\tau_{\max} - \tau_{\min})t + \tau_{\min} \quad (14)$$

the model outputs are transformed to the original time and value scale as follows:

$$\hat{f}(t) \leftarrow \hat{f}(t) \frac{y_{\max} - y_{\min}}{\tau_{\max} - \tau_{\min}} \quad (15)$$

$$\log \text{Var}(\hat{f})(t) \leftarrow \log \text{Var}(\hat{f})(t) + 2 \log \frac{y_{\max} - y_{\min}}{\tau_{\max} - \tau_{\min}} \quad (16)$$

$$\hat{x}_0 \leftarrow \hat{x}_0 (y_{\max} - y_{\min}) + y_{\min} \quad (17)$$

$$\log \text{Var}(\hat{x}_0) \leftarrow \log \text{Var}(\hat{x}_0) + 2 \log (y_{\max} - y_{\min}) \quad (18)$$

While the transformations of \hat{x}_0 and $\log \text{Var}(\hat{x}_0)$ follow immediately from the value renormalization map, the transformations of $\hat{f}(t)$ and $\text{Var}(\hat{f})(t)$ follow from the linearity of the derivative (in case of the value renormalization map) and the chain rule (in case of the time renormalization map).

This described instance normalization approach enables FIM- ℓ to be used in a range of (real-world) applications, as we show in our experiments (Section 4). But there are also limitations, which we will now address.

Firstly, some *signal-to-noise ratio patterns* are not accurately resolved because of this normalization. For example, observations of (almost) constant functions with additive noise are not interpolated very accurately, because the normalization parameters are mainly determined by the noise, not the underlying signal.

Secondly, the internal embeddings of FIM- ℓ do not contain any *information about the scale* of the input. Downstream tasks, like *imputation of temporal missing patterns* could benefit from this information. In such scenarios, we opted for separate embeddings of statistics about the input data scales, to reintroduce them alongside the FIM- ℓ embeddings (see Appendix C.2).

B.2 MODEL ARCHITECTURE

Let us provide more details about the interpolation model architecture, which was already outlined in Section 3.2.1, and hyperparameters of the single FIM- ℓ model all experimental results were derived with. Note that we use SeLU (Klambauer et al., 2017) as activation for all feed-forward neural networks and employ a dropout rate of 0.1.

In total, FIM- ℓ has roughly 20 million learnable parameters. The results of an ablation study on architecture and hyperparameter choices are described in Appendix B.5.

Model inputs:

- (i) A noisy time series $(y_1, \tau_1), \dots, (y_l, \tau_l)$ with observation values $y_i \in \mathbb{R}$ and ordered, but potentially irregular, observation times $\tau_i \in \mathbb{R}_+$ with $\tau_1 < \dots < \tau_l$.
- (ii) A time $t \in \mathbb{R}_+$ at which to evaluate the functions \hat{f} and $\log \text{Var}(\hat{f})$ at.

Model architecture:

- (i) *Temporal embedding.* We use the learnable time embedding from Shukla & Marlin (2020) with output in \mathbb{R}^{512} . Its i th dimension is defined as

$$\phi_0^\theta(t)[i] = \begin{cases} w_0 t + b_0 & \text{if } i = 0 \\ \sin(w_i t + b_i) & \text{otherwise} \end{cases}$$

where w_i and b_i are learnable parameters.

- (ii) *Trunk net equivalent:* We use the time embedding ϕ_0^θ in combination with a feed-forward neural network ϕ_1^θ , with 4x1024 hidden layers and output in \mathbb{R}^{512} , to encode the evaluation time t . The composition $\phi_1^\theta \circ \phi_0^\theta$ can thus be understood as the Trunk net of DeepOnet. Let us denote

$$\mathbf{t}^\theta = (\phi_1^\theta \circ \phi_0^\theta)(t)$$

- (iii) *Individual observations embedding.* Let us denote the i th element of the time series in our input with

$$\mathbf{y}_i^\theta = \text{Concat}(y_i, \phi_0^\theta(\tau_i)).$$

- (iv) *Branch net equivalent.* The embedded time series processing network, which can be understood as the branch net of DeepONets, is a composition of a sequence processing network ψ_1^θ and a feed-forward neural network ϕ_2^θ . The sequence processing network ψ_1^θ is defined as a bi-directional LSTM with hidden states in \mathbb{R}^{512} . The feed-forward neural network ϕ_2^θ with 4x1024 hidden layers and outputs in \mathbb{R}^{512} . Let us denote

$$\mathbf{u}^\theta = \phi_2^\theta(\psi_1^\theta(\mathbf{y}_1^\theta, \dots, \mathbf{y}_l^\theta)).$$

- (v) *Time derivative projection.* We combine the output of the trunk net and branch net equivalent networks via a feed-forward neural network ϕ_3^θ with 4x1024 hidden layers and outputs in \mathbb{R}^{512} . Let us denote its output by

$$\mathbf{h}^\theta(t) = \phi_3^\theta(\text{Concat}(\mathbf{t}^\theta, \mathbf{u}^\theta)).$$

The Gaussian distribution over the values of the estimated time derivative is parameterized by two linear projections from $\mathbf{h}^\theta(t)$ to \mathbb{R} , denoted by

$$\hat{f}(t) = \phi_4^\theta(\mathbf{h}^\theta(t)) \quad \text{and} \quad \log \text{Var}(\hat{f})(t) = \phi_5^\theta(\mathbf{h}^\theta(t)).$$

- (vi) *Initial condition projection:* Parameters of the Gaussian distribution for the initial condition

$$\hat{x}_0 = \phi_6^\theta(\mathbf{u}^\theta) \quad \text{and} \quad \log \text{Var}(\hat{x}_0) = \phi_7^\theta(\mathbf{u}^\theta)$$

are modeled with feed-forward neural networks ϕ_6^θ and ϕ_7^θ each with 4x1024 hidden layers and outputs in \mathbb{R} .

Model outputs: To summarize, our model returns

- (i) a *time derivative* $\hat{f}(t)$, with uncertainty estimate $\log \text{Var}(\hat{f})(t)$, for a time $t \in \mathbb{R}_+$ and
- (ii) a *initial value* \hat{x}_0 , with uncertainty estimate $\log \text{Var}(\hat{x}_0)$.

Combined, these outputs define a function $\hat{x}(\tau)$ interpolating the noisy (input) time series $(y_1, \tau_1), \dots, (y_l, \tau_l)$:

$$\hat{x}(\tau) = \hat{x}_0 + \int_0^\tau \hat{f}(s) ds$$

B.3 TRAINING OBJECTIVE

The parameter set θ of FIM- ℓ is trained in a supervised fashion, utilising the synthetic dataset for *point-wise missing patterns* introduced in Appendix A.

Following the notation of Appendix A.4, let f be the sampled function from one instance in the synthetic dataset, $\{f(t_i)\}_{i=1}^L$ its values on the fine grid, x_0 the initial value of the ODE solution, recorded on the fine grid $\{x(t_i)\}_{i=1}^L$, and $\{(y_i, \tau_i)\}_{i=1}^L$ the associated noisy time series. Using $\{(y_i, \tau_i)\}_{i=1}^L$ as inputs for FIM- ℓ , we denote its outputs by \hat{f} , $\log \text{Var}(\hat{f})$, \hat{x}_0 and $\log \text{Var}(\hat{x}_0)$ as in Appendix B.2.

The training objective of FIM- ℓ consists of three parts:

- (i) Maximizing the Gaussian log-likelihood $\log \mathcal{L}(f(t_i) \mid \hat{f}(t_i), \text{Var}(\hat{f})(t_i))$ of the *time derivative* at all L points t_i of the fine grid.
- (ii) Minimizing the one-step-ahead reconstruction error $|x(t_{i+1}) - (x(t_i) + \hat{f}(t_i)(t_{i+1} - t_i))|$ of the *ODE solution* at $L - 1$ points on the fine grid.
- (iii) Maximizing the Gaussian log-likelihood $\log \mathcal{L}(x_0 \mid \hat{x}_0, \text{Var}(\hat{x}_0))$ of the *initial value*.

Expressed as an equation, we train FIM- ℓ to minimize

$$\begin{aligned} \mathcal{L} = & - \mathbb{E}_{f \sim p(f, \eta_f)} \left\{ \sum_{i=1}^L \frac{(f(t_i) - \hat{f}(t_i))^2}{2\text{Var}(\hat{f})(t_i)} + \frac{1}{2} \log(\text{Var}(\hat{f})(t_i)) \right\} \\ & + \mathbb{E}_{\substack{f \sim p(f, \eta_f) \\ x_0 \sim p(x_0)}} \left\{ \sum_{i=1}^{L-1} |x(t_{i+1}) - (x(t_i) + \hat{f}(t_i)(t_{i+1} - t_i))| \right\} \\ & - \mathbb{E}_{x_0 \sim p(x_0)} \left\{ \frac{(x_0 - \hat{x}_0)^2}{2\text{Var}(\hat{x}_0)} + \frac{1}{2} \log(\text{Var}(\hat{x}_0)) \right\}. \end{aligned}$$

Note that the one-step-ahead reconstruction error is simply the absolute error of a single step of the Euler method, when using the *inferred* time derivative $\hat{f}(t_i)$, but the *ground-truth* starting point $x(t_i)$. Such term is only viable in our supervised training regime on synthetically generated data, where we have access to the ground-truth ODE solution x .

B.4 TRAINING PROCEDURE AND IMPLEMENTATION

The parameters θ of FIM- ℓ were optimized with AdamW (Loshchilov & Hutter, 2017), using a learning rate of $1e^{-6}$ and weight decay $1e^{-4}$. Using a batch size of 1024, the loss on a validation set converged after approximately 500 epochs.

We used four A100 80GB GPUs to train FIM- ℓ . The implementation is done in Jax⁶. Its code and the trained model weights are provided in the supplementary material.

B.5 ABLATION STUDIES: ARCHITECTURE AND DATASET DESIGN

In this section, we present ablation studies of the design of the synthetic training dataset and the architecture of FIM- ℓ . We evaluate the ablations by the R^2 -accuracy on the ODEBench dataset, corrupted with $\rho = 0.5$, $\sigma = 0.05$ (see Appendix E.3 for more details). It is important to note that these models are trained *only* on synthetic data, and *not* on the ODEBench dataset, in accordance with our zero-shot approach.

First, we experiment with the size of our model (2M, 20M, 50M parameters) and the number of trajectories in the the training dataset (2M, 8M trajectories) and summarize the results in Table 4. For 2M trajectories, increasing the number of parameters from 2M to 50M does increase the

⁶<https://jax.readthedocs.io/en/latest/index.html>

performance by around 4%. For 8M trajectories, the trend persists with the 20M parameter model, but reverts with the 50M parameter model, resulting in no significant improvement.

Next, we experiment with the architecture of the sequence processing network ψ_1^θ , considering BiLSTM and transformer networks. The results are presented in Table 5 and show that there is no significant difference in performance when evaluated on the ODEBench dataset.

Table 4: R^2 accuracy with standard deviation, ablating parameter count and number of time series in train set.

Parameters	Time Series in Train Set	
	2M	8M
2M	82.6 ± 0.7	82.3 ± 0.9
20M	87.3 ± 1.3	86.2 ± 1.0
50M	87.7 ± 2.0	84.1 ± 1.3

Table 5: R^2 Accuracy with standard deviation, ablating the architecture of the sequence processing network ψ_1^θ .

ψ_1^θ Architecture	R^2 Accuracy (%)
BiLSTM	87.30 ± 1.35
Transformer	87.38 ± 1.42

An additional study we conducted involves varying the size of the maximum and minimum training contexts points in a time series of the synthetic train set, which we denote by L_{\max} and L_{\min} . The results for ablating L_{\max} , presented in Table 6, indicate that, at least on the ODEBench dataset, the model performs better with more context points. However, the results are within error bars. Similarly, the results for ablating L_{\min} , shown in Table 7, reveal that the model performs better when only trained on time series with more observations. Again, this result is only valid for the ODEBench dataset, as other applications *require small context windows*, e.g. because there are too few observations in the time series.

Table 6: R^2 Accuracy with standard deviation, ablating L_{\max} , the maximum number of observations in a time series of the synthetic train dataset.

L_{\max}	R^2 Accuracy (%)
128	87.3 ± 1.3
64	86.7 ± 1.2

Table 7: R^2 accuracy with standard deviation, ablating L_{\min} , the minimum number of observations in a time series of the synthetic train dataset.

L_{\min}	R^2 Accuracy (%)
8	87.3 ± 1.3
32	89.0 ± 1.0

B.6 PROCESSING TIME SERIES OF ANY LENGTH AND DIMENSIONALITY

As a *zero-shot* inference model, FIM- ℓ should be able to cope with dynamic phenomena of very diverse nature. In particular, it should handle observations with different dimensionalities, lengths and scales. Our approach to handle different scales with instance normalization was discussed in Appendix B.1. Now we want to address our approach to the other two phenomena and offer some limitation of these approaches.

B.6.1 COMPOSITION ACROSS DIMENSIONS

To handle different (in fact, arbitrary) dimensional observations, we process each feature of a time series separately with our pretrained model FIM- ℓ . The synthetic training dataset only contains 1D time series (see Appendix A.1) and the model architecture only returns 1D time derivatives (see Appendix B.2). Such channel independent strategy has been used previously, e.g. by Nie et al. (2023) and Han et al. (2024).

Regarding the inference problem of the *time derivative on a ODE solution path*, this reduction to 1D systems is *exact*, not an approximation. Indeed, consider a vector field $\mathbf{f} : \mathbb{R}^+ \times \mathbb{R}^D \rightarrow \mathbb{R}^D$ and the solution $\mathbf{x} : \mathbb{R}^+ \rightarrow \mathbb{R}^D$ to some initial value problem (x_0, \mathbf{f}) . Then its time derivative, i.e. the vector field along the solution path, $\mathbf{f}(t, \mathbf{x}(t))$ is a purely time-dependent function, which naturally splits into D independent coordinate functions $(\mathbf{f}_1(t, \mathbf{x}(t)), \dots, \mathbf{f}_D(t, \mathbf{x}(t)))$.

Coordinates of datasets generated from *real-world scenarios*, which we consider in our experiments, might not be independent or uncorrelated. Still, we show that our approach can perform well in a va-

riety of such scenarios. However, extreme cases like the PHYSIONET2012 dataset (Du et al., 2024), with very sparse observations in some coordinates, are a natural limitation of channel independent approaches like ours.

B.6.2 COMPOSITION ALONG TIME

Time series in the training set of FIM- ℓ are bounded in length by a fixed upper bound L_{max} , as described in Section 3.1. Therefore, FIM- ℓ can only (reasonably) process time series which lengths do not exceed this upper bound. Similarly, FIM- ℓ can only (reasonably) infer time derivatives approximately contained in the broad distributions over parametric functions of time, specified in Appendix A.1.

Datasets from *real-world* scenarios will likely not adhere to these limitations derived from our synthetic training dataset.

To adapt the *pretrained* FIM- ℓ to handle such scenarios, we employ a *windowing scheme*. Concretely, we split the time series into successive, overlapping windows that are still processable by the FIM- ℓ . Applying (instances of) FIM- ℓ to each window individually yields local estimates of the solution $\hat{x}(t)$.

As windows are processed separately, instance normalization (see Appendix B.1) and corresponding renormalization occurs individually at their respective scales.

To get a global estimate out of the local estimates, one can combine them on the overlaps with two approaches.

1. *Interpolating the ODE solutions.* Consider two successive, overlapping time windows A and B , defined on the intervals $[t_0^A, t_1^A]$ and $[t_0^B, t_1^B]$, respectively, so that

$$0 \leq t_0^A < t_0^B < t_1^A < t_1^B.$$

Applying an instance of FIM- ℓ to each window yields local solutions $\hat{x}_A(t)$ and $\hat{x}_B(t)$ in the respective windows. By defining

$$\hat{x}(t) = \begin{cases} \hat{x}_A(t), & \text{if } t < t_0^B \\ \frac{t_1^A - t}{t_1^A - t_0^B} \hat{x}_A(t) + \frac{t - t_0^B}{t_1^A - t_0^B} \hat{x}_B(t), & \text{if } t_0^B \leq t \leq t_1^A \\ \hat{x}_B(t), & \text{if } t > t_1^A \end{cases} \quad (19)$$

for $t \in [t_0^A, t_1^B]$, we combine $\hat{x}_A(t)$ and $\hat{x}_B(t)$ to a global solution $\hat{x}(t)$ with linear interpolation on the overlap. The time derivative \hat{f} corresponding to \hat{x} can be found (*a.e.*) by taking the derivative of equation 19.

2. *Interpolating the time derivatives and solving the ODE.* Alternatively we could interpolate the estimated time derivatives $\hat{f}_A(t)$ and $\hat{f}_B(t)$ of the time windows A and B , just as done in Eq. 19 but with \hat{x} replaced with \hat{f} . Once such an interpolated time derivative is available one can integrate the ODE over the complete interval $[t_0^A, t_1^B]$. However, this second approach accumulates the errors of the ODE solutions of each interval.

In practice, and for all experiments described in Section 4 and the Appendix, we used the first approach.

Notation. There are two methods for specifying the overlapping windows:

1. Windows specified by the *number of windows* that cover the observations. For m windows we write FIM- $\ell(w.n. = m)$, identifying this method.
2. Windows specified by the *number of observations* they contain. For m observations per windows, we write FIM- $\ell(o.n. = m)$, identifying this method.

Limitations. Our experiments in Section 4 show that our compositional approach along time can be quite effective. Still, there are natural limitations, which we want address.

Firstly, although our distributions over parametric functions of time are broad, they do not cover all local patterns exhibited by real-world time series. For example, FIM- ℓ struggles with high-frequency time series with sparse observations. Many windows are required to accurately interpolate

such patterns. Future work will explore the design of the synthetic training data distributions, to cover more of these patterns with $\text{FIM-}\ell$

Secondly, (subsequent) temporal missing patterns can not be accurately imputed with the windowing approach. As windows are processed individually, and their outputs merged manually on the overlaps, no information is passed between them. Therefore, imputation that requires global, long range patterns can not be resolved. We handle the *temporal missing pattern imputation* with an additional imputation module in FIM (see Appendix C).

C FIM FOR INTERPOLATING TEMPORAL MISSING PATTERNS: ADDITIONAL DETAILS

C.1 INPUT PREP-PROCESSING AND OUTPUT POST-PROCESSING

Analogous to the local interpolation model discussed in Appendix B, our zero-shot model for interpolating temporal missing patterns FIM should accommodate time series of all scales. Hence, we again employ min-max-normalization for the observation values *per time series*, as described for $\text{FIM-}\ell$ in Appendix B.1.

Our approach to the *temporal missing pattern* imputation task involves one more step of instance normalization, which we want to address now. For this sake, let us briefly recall the notation introduced in Section 3.2.2. A (ordered) time series with observations $\{(y_i, \tau_i)\}_{i=0}^l$ is split into K sequentially ordered sets

$$y_1, \dots, y_{w_1} \cup y_{w_1+1}, \dots, y_{w_1+w_2} \cup \dots \cup y_{l-w_l+1}, \dots, y_l,$$

where the q th set is empty, meaning it contains no observations, but defines a consecutive time range, which we call the *time gap*. Our goal is to impute values in this gap.

Recall that one part of our model (described in Section 3.2.2 and Appendix C.2) applies a *pretrained* $\text{FIM-}\ell$ to all sets, except the q th. Internally, $\text{FIM-}\ell$ normalizes each set *locally*, processes it and renormalizes its outputs accordingly. In the crucial part of our approach, the model predicts an embedding \mathbf{u}_q for the q th set, which is processed with $\text{FIM-}\ell$, to return \hat{f} , $\log \text{Var}(\hat{f})$ and \hat{x}_0 *inside the gap*.

It is only possible to *locally renormalize* these outputs wrt. the time range of the gap, because there are no observation values. The *global* renormalization is not effected by this deficit, because on this scale, the predicted output at the gap is renormalized with the *global normalization parameters*, equivalent to the outputs at all other sets.

Because the model is subjected to this deficit during training, and inputs are instance normalized globally, the model learns to adjust to these conditions.

C.2 MODEL ARCHITECTURE

Let us provide more details about the architecture of FIM , the imputation model for *temporal missing patterns*, which was already outlined in Section 3.2.2 and hyperparameters of the single FIM model all experimental results were derived with. Following the model architecture of $\text{FIM-}\ell$ (see Appendix B.2), we use SeLU (Klambauer et al., 2017) as activation for all feed-forward neural networks and employ a dropout rate of 0.1.

FIM contains a pretrained $\text{FIM-}\ell$ model, which parameters θ are frozen. Additionally, FIM has roughly 6M trainable parameters, which we denote by φ .

Model inputs:

- (i) A noisy time series $(y_1, \tau_1), \dots, (y_l, \tau_l)$ with observation values $y_i \in \mathbb{R}$ and ordered, but potentially irregular, observation times $\tau_i \in \mathbb{R}_+$ with $\tau_1 < \dots < \tau_l$.
- (ii) An ordered splitting of the interval $[\tau_1, \tau_l]$ into $K = 5$ sequentially ordered sets, which induces a splitting of the observations into K sets

$$y_1, \dots, y_{w_1} \cup y_{w_1+1}, \dots, y_{w_1+w_2} \cup \dots \cup y_{l-w_l+1}, \dots, y_l,$$

where the q th set only defines a consecutive time range (or *imputation gap*) and does not contain any actual observations.

- (iii) A time $t \in \mathbb{R}_+$ in the imputation gap at which to evaluate the functions \hat{f} and $\log \text{Var}(\hat{f})$ at.

Model architecture:

- (i) *Local scale statistics.* Defining $w_0 = 0$ and $w_j^{\text{prev}} = \sum_{k=0}^{j-1} w_k$ for convenience, we set

$$\begin{aligned} y_j^{\min} &= \min_{i=1, \dots, w_j} y_{w_j^{\text{prev}}+i} & y_j^{\max} &= \max_{i=1, \dots, w_j} y_{w_j^{\text{prev}}+i} & y_j^{\text{range}} &= y_j^{\max} - y_j^{\min} \\ y_j^{\text{first}} &= y_{w_j^{\text{prev}}+1} & y_j^{\text{last}} &= y_{w_j^{\text{prev}}+w_j} & y_j^{\text{diff}} &= y_j^{\text{last}} - y_j^{\text{first}} \\ \tau_j^{\text{first}} &= \tau_{w_j^{\text{prev}}+1} & \tau_j^{\text{last}} &= \tau_{w_j^{\text{prev}}+w_j} & \tau_j^{\text{diff}} &= \tau_j^{\text{last}} - \tau_j^{\text{first}} \end{aligned}$$

and denote by

$$s_j = [y_j^{\min}, y_j^{\max}, y_j^{\text{range}}, y_j^{\text{first}}, y_j^{\text{last}}, y_j^{\text{diff}}, \tau_j^{\text{first}}, \tau_j^{\text{last}}, \tau_j^{\text{diff}}] \in \mathbb{R}^9$$

the statistics about the *position* and *local scale* for the j th set, where $j \neq q$.

- (ii) *Local scale embedding.* A learnable linear layer ϕ_8^φ embeds the local scale statistics s_j for all $j \neq q$. Let us denote

$$\mathbf{s}_j^\varphi = \phi_8^\varphi(s_j) \in \mathbb{R}^{512}.$$

As mentioned in Appendix C.1, we also have access to the boundary times of the imputation gap: τ_q^{first} , τ_q^{last} and τ_q^{diff} . We can thus *locally* time instance normalize t as $t \leftarrow (t - \tau_q^{\text{first}}) / \tau_q^{\text{diff}}$, such that it is on the correct scale to apply the Trunk net of the pretrained FIM- ℓ . Let us again denote the output of the Trunk net as $\mathbf{t}^\theta = (\phi_1^\theta \circ \phi_0^\theta)(t)$.

- (iii) *FIM- ℓ embedding.* We apply the temporal encoder ϕ_0^θ and the Branch net equivalent network $\phi_2^\theta \circ \psi_1^\theta$ of the underlying, *pretrained* FIM- ℓ model to all sets $j \neq q$. Concretely, ϕ_0^θ yields the individual observation embeddings

$$\mathbf{y}_i^\theta = \text{Concat}(y_i, \phi_0^\theta(\tau_i)) \in \mathbb{R}^{513} \quad \text{for all } i = 1, \dots, l,$$

and $\phi_2^\theta \circ \psi_1^\theta$ yields

$$\mathbf{u}_j^\theta = \phi_2^\theta(\psi_1^\theta(\mathbf{y}_{w_j^{\text{prev}}+1}^\theta, \dots, \mathbf{y}_{w_j^{\text{prev}}+w_j}^\theta)) \in \mathbb{R}^{512} \quad \text{for all } j \neq q.$$

- (iv) *Gap embedding estimation.* A sequence processing network ψ_2^φ , a transformer with 4 layers, 8 heads and (self) attention dimension 512, processes the sequence

$$(\mathbf{u}_1^\theta, \mathbf{s}_1^\varphi), \dots, (\mathbf{u}_{q-1}^\theta, \mathbf{s}_{q-1}^\varphi), (\mathbf{u}_{q+1}^\theta, \mathbf{s}_{q+1}^\varphi), \dots, (\mathbf{u}_K^\theta, \mathbf{s}_K^\varphi)$$

and returns an embedding for the q th set, that is

$$\mathbf{u}_q^\varphi = \psi_2^\varphi((\mathbf{u}_1^\theta, \mathbf{s}_1^\varphi), \dots, (\mathbf{u}_{q-1}^\theta, \mathbf{s}_{q-1}^\varphi), (\mathbf{u}_{q+1}^\theta, \mathbf{s}_{q+1}^\varphi), \dots, (\mathbf{u}_K^\theta, \mathbf{s}_K^\varphi)) \in \mathbb{R}^{512}.$$

- (v) *FIM- ℓ time derivative projection.* We apply feed-forward neural networks ϕ_3^θ , ϕ_4^θ and ϕ_5^θ of the underlying, *pretrained* FIM- ℓ model to the estimated embedding \mathbf{u}_q^φ and the time t in the imputation gap. We write

$$\hat{f}_q(t) = \phi_4^\theta(\mathbf{h}_q^\varphi(t)), \quad \log \text{Var}(\hat{f}_q)(t) = \phi_5^\theta(\mathbf{h}_q^\varphi(t)), \quad \text{with } \mathbf{h}_q^\varphi(t) = \phi_3(\mathbf{t}^\theta, \mathbf{u}_q^\varphi).$$

Finally, we revert the *local* time instance normalization from (ii) inside the imputation gap, with the formulas presented in Appendix B.1.

Model outputs: In conclusion, our model returns a *time derivative* $\hat{f}_q(t)$, with uncertainty estimate $\log \text{Var}(\hat{f}_q)(t)$, for a time $t \in \mathbb{R}_+$ in the evaluation gap.

Let us note in passing that the intermediate embeddings \mathbf{u}_j^θ for $j \neq q$ can be processed as usual with the underlying FIM- ℓ . Therefore, the *temporal missing pattern imputation model* can also return $\hat{f}_j(t)$, $\log \text{Var}(\hat{f}_j)(t)$ and initial conditions for sets $j \neq q$, via applications of the underlying FIM- ℓ . In Appendix C.6 we discuss how to combine these outputs from all K sets to infer a continuous interpolating path $\hat{x}(t)$ defined on $[0, 1]$.

C.3 TRAINING OBJECTIVE

The parameters φ of FIM are trained in a supervised fashion, utilising the synthetic dataset for *temporal missing patterns* introduced in Appendix A.

We briefly recall the notation of Appendix A.4 for the data generated by the synthetic dataset. Let f be the sampled function from one instance in the synthetic dataset, $\{f(t_i)\}_{i=1}^L$ its values on the fine grid, x_0 the initial value of the ODE solution, recorded on the fine grid $\{x(t_i)\}_{i=1}^L$, and $\{(y_i, \tau_i)\}_{i=1}^L$ the associated noisy time series.

The noisy time series is split into K sequentially ordered sets, as outlined in Appendix C.2. Following the notation therein, we can identify the subset

$$\{t_i^q\}_{i=1}^M = \{t_i \mid \tau_q^{\text{first}} \leq t_i \leq \tau_q^{\text{last}}\} \subseteq \{t_i\}_{i=1}^L$$

of points on the fine grid contained in the imputation window.

Using $\{(y_i, \tau_i)\}_{i=1}^L$ as inputs for FIM, we denote its outputs evaluated on fine grid points contained in the imputation window by $\hat{f}(t_i^q)$ and $\log \text{Var}(\hat{f})(t_i^q)$, as in Appendix C.2.

The training objective of FIM is then to maximize the Gaussian log-likelihood of the *time derivative* $\log \mathcal{L}(f(t_i^q) \mid \hat{f}(t_i^q), \text{Var}(\hat{f})(t_i^q))$ at all M points t_i^q of the fine grid contained in the imputation gap.

Expressed as an equation, we train FIM to minimize

$$\mathcal{L} = - \mathbb{E}_{f \sim p(f, \eta_f)} \left\{ \sum_{i=1}^M \frac{(f(t_i^q) - \hat{f}(t_i^q))^2}{2\text{Var}(\hat{f})(t_i^q)} + \frac{1}{2} \log(\text{Var}(\hat{f})(t_i^q)) \right\}.$$

C.4 TRAINING PROCEDURE

The parameters φ of FIM were optimized with AdamW (Loshchilov & Hutter, 2017), using a weight decay of $1e^{-3}$. We use a cosine annealing schedule as introduced by Loshchilov & Hutter (2016), where the learning rate decays from $1e^{-4}$ to $1e^{-7}$ over 400 epochs. Note that we do not deploy warm restarts. With a batch size of 1024, we trained FIM on a single A100 80GP GPU.

C.5 ABLATION STUDIES: DATASET DESIGN

The dataset is generated using a GP model with periodic kernels. The grid spans from 0 to 1 with a resolution of 512 points. Each GP is created by combining kernels, and the parameters are sampled from uniform distributions. The lengthscale ℓ is sampled from $\mathcal{U}(0.75, 1)$, while the period is sampled from $\mathcal{U}(0.3, 0.5)$. The training dataset contains 500,000 samples and the test dataset contains 50,000 samples.

Our experimental datasets for the temporal missing pattern imputation (see Appendix G) contain no significant trends. Moreover, the temporal size of the imputation gap is 20% for all samples in the time series. Yet our synthetic generated training data includes both: trends and variable window sizes.

To assess the impact of the trend in our synthetic generated training data on the evaluation performance, we train two sets of models: one with a trend in the training data and the other without a trend. For both datasets, we train two models, varying the size of the imputation window. Specifically, the window size is sampled from either $\mathcal{U}(10, 30)$ or $\mathcal{U}(5, 50)$. In Table 8 we present the results of the four different FIM models trained on the four different dataset. One can see that the model trained on the dataset with smaller imputation window performs the best. Increasing the imputation window size leads to worse performance on the Motion Capture dataset for both case (PCA and no PCA). The performance of the FIM model also decreases when trend is included in the training dataset.

C.6 CONTINUITY ALONG THE GAP

Similar to the windowing scheme of FIM- ℓ (see Appendix B.6.2), FIM processes a time series split into K sets of sequentially ordered observations. Continuing the notation from Appendix C.2, we

Table 8: Ablation study on the size of the imputation window size and the occurrence of trends in the synthetic training data of FIM. We report RMSE in the imputation gap of the Motion Capture dataset.

Dataset	Motion Capture	
	PCA	No PCA
No Trend - $\mathcal{U}(10, 30)$	3.27 ± 1.12	2.97 ± 0.96
Trend - $\mathcal{U}(10, 30)$	3.41 ± 1.17	3.16 ± 1.07
No Trend - $\mathcal{U}(5, 50)$	3.59 ± 1.14	3.52 ± 1.18
Trend - $\mathcal{U}(5, 50)$	3.67 ± 1.13	3.59 ± 1.19

now detail our approach to connecting these outputs, such that the combined interpolating path $\hat{x}(t)$ is continuous in $[0, 1]$.

We can group sets containing observations, i.e. $j \neq q$ outside of the imputation gap, into two disjoint groups: sets $1 \leq j < q$ to the *left* of the imputation window and sets $q < j \leq K$ to the *right* of the imputation window. Model outputs for each group can be combined with the ideas from FIM- ℓ , presented in Appendix B.6.2. Indeed, these sets are just windows that can be combined on some predefined overlap.

Let \hat{x}^{left} and \hat{x}^{right} denote the inferred trajectories to the left and right of the imputation gap $[\tau_q^{\text{first}}, \tau_q^{\text{last}}]$, which are designed to be *continuous* by the efforts described in Appendix B.6.2. To connect the two trajectories to a continuous path inside the imputation gap, we first extend both of them individually by integrating the time derivative \hat{f}_q inferred from FIM with initial values \hat{x}^{left} and \hat{x}^{right} respectively.

Expressed in equations, we define for $t \in [\tau_q^{\text{first}}, \tau_q^{\text{last}}]$ the following extensions:

$$\begin{aligned}\hat{x}^{\text{left}}(t) &= \hat{x}^{\text{left}}(\tau_q^{\text{first}}) + \int_{\tau_q^{\text{first}}}^t \hat{f}_q(s) ds \\ \hat{x}^{\text{right}}(t) &= \hat{x}^{\text{right}}(\tau_q^{\text{last}}) - \int_t^{\tau_q^{\text{last}}} \hat{f}_q(s) ds\end{aligned}$$

These extensions are then combined via weighted temporal interpolation, where we define the combined solution at a time $t \in [0, 1]$ by

$$\hat{x}(t) = \begin{cases} \hat{x}^{\text{left}}(t) & \text{for } t < \tau_q^{\text{first}} \\ \frac{\tau_q^{\text{last}} - t}{\tau_q^{\text{last}} - \tau_q^{\text{first}}} \hat{x}^{\text{left}}(t) + \frac{t - \tau_q^{\text{first}}}{\tau_q^{\text{last}} - \tau_q^{\text{first}}} \hat{x}^{\text{right}}(t) & \text{for } t \in [\tau_q^{\text{first}}, \tau_q^{\text{last}}] \\ \hat{x}^{\text{right}}(t) & \text{for } t > \tau_q^{\text{last}}. \end{cases} \quad (20)$$

Note that \hat{x} is *continuous by design* and its corresponding combined time derivative \hat{f} can be found (*a.e.*) by taking the derivative of equation 20.

C.7 PROCESSING TIME SERIES OF ANY DIMENSIONALITY

FIM contains a pretrained FIM- ℓ model. In fact, FIM just extends that (frozen) model by two networks: a linear layer ϕ_8 to embed local scale statistics, and a sequence processing network ψ_2 , processing a sequence of FIM- ℓ embeddings of sets of (consecutive) observations. Therefore, it also only returns 1D time derivatives. To impute arbitrary dimensional time series data with FIM, we process each component of a time series separately. The same channel independent strategy is used for FIM- ℓ . In Appendix B.6.1 we discuss limitations of this approach, which are also valid for the temporal missing pattern imputation model FIM.

D EVALUATION METRICS

Depending on the experiment and the baselines, we use one or more of the following evaluation metrics for multi-dimensional time series.

Following the notation of Du et al. (2024), consider a multi-dimensional target time series x_1, \dots, x_L , with $x_i \in \mathbb{R}^D$, and corresponding estimated time series $\hat{x}_1, \dots, \hat{x}_L$. Some baselines only compute the metrics below on certain elements and components of each time series. Let m_1, \dots, m_L be an associated sequence of masks $m_i \in \{0, 1\}^D$, indicating which elements and components are part of the metric calculation. Finally, denote by x_i^d, \hat{x}_i^d and m_i^d the d th component of each vector.

We compute per trajectory the Mean Absolute Error (MAE), (Root) Mean Squared Error ((R)MSE), Mean Relative Error (MRE) and the R^2 score, defined as follows:

$$\begin{aligned} \text{MAE}(x, \hat{x}, m) &= \frac{\sum_{i=1}^L \sum_{d=1}^D |x_i^d - \hat{x}_i^d| \cdot m_i^d}{\sum_{i=1}^L \sum_{d=1}^D m_i^d} \\ \text{MSE}(x, \hat{x}, m) &= \frac{\sum_{i=1}^L \sum_{d=1}^D (x_i^d - \hat{x}_i^d)^2 \cdot m_i^d}{\sum_{i=1}^L \sum_{d=1}^D m_i^d} \\ \text{RMSE}(x, \hat{x}, m) &= \sqrt{\text{MSE}(x, \hat{x}, m)} \\ \text{MRE}(x, \hat{x}, m) &= \frac{\sum_{i=1}^L \sum_{d=1}^D |x_i^d - \hat{x}_i^d| \cdot m_i^d}{\sum_{i=1}^L \sum_{d=1}^D |x_i^d| \cdot m_i^d} \\ R^2(x, \hat{x}) &= \frac{1}{D} \sum_{d=1}^D \left[1 - \frac{\sum_{i=1}^L (x_i^d - \hat{x}_i^d)^2}{\sum_{i=1}^L (x_i^d - \bar{x}^d)^2} \right] \end{aligned}$$

where $\bar{x}^d = \frac{1}{L} \sum_{i=1}^L x_i^d$. Note that we only require the R^2 score for the comparison on ODEBench, where no targets are masked, so we do not add the mask in the formula above.

For the imputation task of *point-wise missing patterns*, we usually compute the metrics only at the missing points, following the methodology of our baselines, e.g. (Du et al., 2024). One exception is the ODEBench evaluation, where the baseline values are computed against the complete target trajectory, including observed and missing time points. We adapt our computation to the baseline methodology for a valid comparison.

For the imputation task of *temporal missing patterns*, metrics are only computed *in the imputation gap*, in accordance with our baselines.

Usually, we report mean and standard deviation of the metrics calculated over all trajectories in a dataset. The only exception is the R^2 -Accuracy, defined by d'Ascoli et al. (2024) as the percentage of time series with R^2 score larger than 0.9. Note that Du et al. (2024) and Fang et al. (2024a) only report metrics averaged over all missing values over all time series, not a standard deviation over time series.

E PHASE PORTRAIT RECONSTRUCTION: ADDITIONAL RESULTS

E.1 VAN DER POLL OSCILLATOR

E.1.1 DATA DESCRIPTION AND PRE-PROCESSING

One particular (second-order) differential equation from the ODEBench dataset is the Van der Pol oscillator:

$$\begin{aligned} dx &= v \\ dv &= \mu(1 - x^2)v - x \end{aligned}$$

We simulate the system in the time interval $[0, 10]$ for a set of initial positions $x(0)$, initial velocities $v(0)$ and parameters μ :

$$\begin{aligned} x(0) &\in \{-5, -3, -1, 1, 3, 5\} \\ v(0) &\in \{-4.5, 4.5\} \\ \mu &\in \{0.1, 0.5, 1.5\} \end{aligned}$$

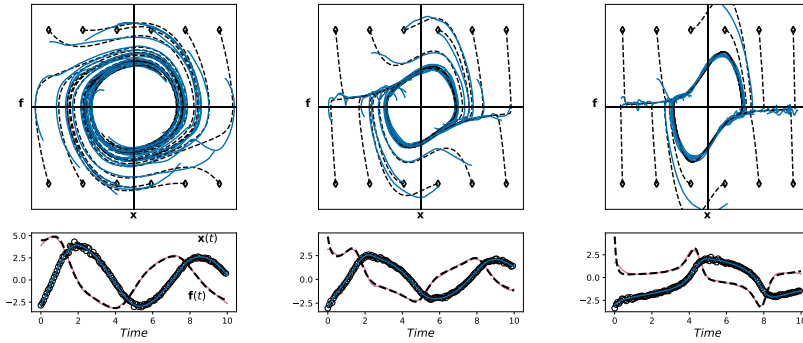


Figure 4: Phase portraits of Van der Pol systems with parameters $\mu = 0.1, 0.5, 1.5$. 128 noisy observation (black circles) get interpolated by $\text{FIM-}\ell(w.n. = 4)$ (blue line). The inferred time derivative matches (magenta line) matches the ground truth vector field at the solution path (black dashed lines).

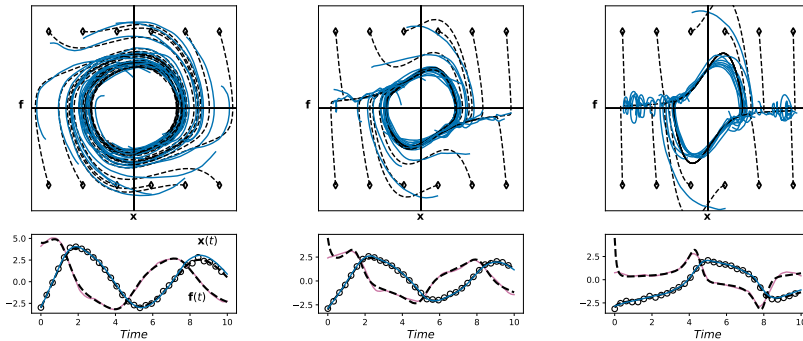


Figure 5: Phase portraits of Van der Pol systems with parameters $\mu = 0.1, 0.5, 1.5$. 32 noisy observation (black circles) get interpolated by $\text{FIM-}\ell(w.n. = 4)$ (blue line). The inferred time derivative matches (magenta line) matches the ground truth vector field at the solution path (black dashed lines).

We generate 1D time series by observing *the position $x(t)$ only* at a regular grid of either 128 or 32 points in the interval $[0, 10]$ and corrupt them with multiplicative noise of level $\gamma = 0.05$ inspired by the ODEBench setup (see Appendix E.3).

E.1.2 MODELLING AND RESULTS

We apply $\text{FIM-}\ell(w.n. = 4)$ and visualise the inferred path and the inferred time derivative by means of phase portraits. Figure 4 contains the visualisation for 128 observations and Figure 5 for 32 observations. In each figure, the parameter μ ranges from $\mu = 0.1$ in the left, to $\mu = 0.5$ in the middle and $\mu = 1.5$ in the right subplot.

$\text{FIM-}\ell$ interpolates the observed path and the inferred time derivative $f(t)$ matches the ground truth vector field $v(t)$ at the path closely. The accuracy of the (implied) estimation $f(0)$ of the initial velocity $v(0)$ is not perfect and degrades with increasing μ . In other words, based purely on the (limited) observations, the model can not infer the sharp change in velocity at the beginning of a trajectory. The bottom, 1D subplots reveal that $\text{FIM-}\ell$ adjusts to a more accurate estimation quickly.

Even with only 32 observations (considerably less than the roughly 256 observations in the ODEBench), $\text{FIM-}\ell$ recovers the ground truth time derivative quite well, showcasing that $\text{FIM-}\ell$ does not require many observations to approximate simpler regions of the dynamics.

E.2 RÖSSLER ATTRACTOR

E.2.1 DATA DESCRIPTION AND PRE-PROCESSING

In Figure 2 we consider the Rössler attractor differential equation from the ODEBench in its chaotic variation:

$$\begin{aligned} dx &= -5(y + z) \\ dy &= 5(0.2y + x) \\ dz &= 5(0.2 + z(-5.7 + x)) \end{aligned}$$

Also following the ODEBench, we simulate the system in the time interval $[0, 10]$ with initial value $(2.3, 1.1, 0.8)$. From 4096 observations on a regular time grid in $[0, 10]$, we subsample a irregular observation grid by dropping each observation (independently) with probability 0.5. The subsampled data is then corrupted with multiplicative noise of level 0.05. This corruption scheme follows one corruption scheme of ODEBench, which is described in see Appendix E.3.

E.2.2 MODELLING AND RESULTS

We apply $\text{FIM-}\ell(w.n. = 32)$ to recover the trajectory from the corrupted data. Our model also returns the time derivative along the recovered trajectory, which is the velocity of the particle in the Rössler attractor system. The centered plot in Figure 2 shows the ground-truth and model inference by means of a phase portrait. It contains position and velocity for the first component, i.e. x and dx , along the trajectory.

Our model can also approximate the acceleration of the particle. First, we discretize the *inferred velocity* via a regular grid of size 8192 in the time interval $[0, 10]$. To this discretized function, we apply $\text{FIM-}\ell(w.n. = 64)$ and recover an approximation of the acceleration of the particle. The rightmost plot in Figure 2 shows the velocity and acceleration of the first component along the observed trajectory, again by means of a phase portrait.

E.3 ODE BENCH

E.3.1 DATA DESCRIPTION AND PRE-PROCESSING

The ODEBench dataset (d’Ascoli et al., 2024) contains the solution of 63 ODEs with 2 initial conditions each. The solutions are available on a regular grid of length 512 in the time interval $[0, 10]$.

We follow the pre-processing of d’Ascoli et al. (2024), who corrupt both the observations values and the observation grid. Let us recall their corruption scheme here for completeness.

The *observation values* are corrupted by multiplicative noise, yielding noisy observations y_i of the ground truth solution $x_i = x(t_i)$ at some time t_i via $y_i = (1 + \epsilon)x_i$, where $\epsilon \sim \mathcal{N}(0, \gamma)$. The *observation grid* is corrupted by dropping each observation (independently) with probability ρ .

All combinations of $\gamma \in \{0, 0.05\}$ and $\rho \in \{0, 0.5\}$ are considered.

E.3.2 BASELINES

We are interested in two tasks on this dataset:

- (i) reconstruction of the underlying *ODE solution* (which is the task considered by d’Ascoli et al. (2024)) and
- (ii) inference of the vector field on the solution path, i.e. the *time derivative*.

Note that in the case of $\rho = 0.5$, this setup is very similar to the *missing point imputation* task considered in other works.

While d’Ascoli et al. (2024) consider the first task (and we compare against their results below), they do not report any results related to the second task. We therefore reevaluate ODEFormer on the ODEBench, to gain access to the time derivative information needed for our comparison. We use

the implementation and weights provided by the authors⁷, apply it to 10 samplings of the corruption schemes (as we do for our own model) and average the results.

On the solution reconstruction task, our re-evaluation yields different results than reported by the authors (see e.g. Table 9). We report both results, if they are available, and name the results from our re-evaluation *ODEFormer Re-ev.*

Results of other well performing models on the ODEBench have been extracted from Figure 4 of d’Ascoli et al. (2024).

E.3.3 MODELLING AND RESULTS

We apply $\text{FIM-}\ell$ to all equations of ODEBench and compare our results to the best performing models from d’Ascoli et al. (2024), as well as our re-evaluation of ODEFormer outlined in Appendix E.3.2.

The authors of ODEBench compare several methods based on the reconstruction of the ground-truth ODE solution at all 512 available points of each trajectory. This comparison is based on the R^2 accuracy - the percentage of predictions of which the R^2 score exceeds 0.9. We compare our zero-shot model $\text{FIM-}\ell$ with different numbers of windows to the best performing models from d’Ascoli et al. (2024). We report our result wrt. the R^2 -accuracy (see Table 9), the RMSE (see Table 10) and the MAE (see Table 11). For our models, and if available for ODEFormer, we provide the metrics for equations grouped by their dimensionality, and average our results over 10 samplings of the corruption schemes detailed above.

Averaged over all equations, $\text{FIM-}\ell$ improves the baselines on all corruption schemes, in particular with larger number of windows. The optimal number of windows depends on the difficulty of the underlying solution. More complex dynamics require a higher local resolution, thus more windows, than easier dynamics, which benefit from the smooting effect of a low number of windows. Generally speaking, equations of the same dimensionality in the ODEBench are of similar complexity. We therefore denote by $\text{FIM-}\ell(\text{Weighted Sum})$ the average of the best performing number of windows per equation, weighted by the number of equations of that dimension.

Noticeably, the performance drops for equations of dimension 3. Figure 6 shows the path reconstruction for one initial value problem of each equation. Trajectories of $3D$ systems included in ODEBench are inherently more complex than for all other dimensions. Still, $\text{FIM-}\ell(w.n. = 8)$, used for Figure 6, infers suitable initial conditions and vector fields that approximate the ground-truth solution well.

Let us now consider the accuracy of the inferred time derivative along the solution path. We provide the results for our model and for our re-evaluation of ODEFormer on ODEBench. Similar to the original ODEBench task, we compute the metrics against the time derivative along the solution path of the ground-truth solution. To extract an estimation of the this time derivative from ODEFormer, we can evaluate the inferred equation along two possible paths:

- (i) the *ground-truth* solution of the *ground-truth* equation
- (ii) the *inferred trajectory* from ODEFormer

While we report both evaluation approaches, we find that the second performs consistently better than the first. We mark the results with *ODEFormer (g.t. traj)* and *ODEFormer (inf. traj.)* respectively.

We report the results wrt. the RMSE (see Table 12) and the MAE (see Table 13). Our model performs better than ODEFormer on both evaluation approaches. The inferred time derivative is much closer to the ground-truth vector field along the solution path, especially when we use more than 2 windows.

⁷<https://github.com/sdascoli/odeformer>

Table 9: ODEBench R^2 accuracy of FIM- ℓ for different numbers of window, split by dimensions. The standard deviation is calculated across 10 samplings of the corruption schemes.

Dim.	Model	$\rho = 0$	$\rho = 0$	$\rho = 0.5$	$\rho = 0.5$
		$\gamma = 0$	$\gamma = 0.05$	$\gamma = 0$	$\gamma = 0.05$
All	ODEFormer	71.2	52.2	69.9	60.3
	ODEFormer-opt	75.9	55.7	74.7	66.6
	ODEFormer Re-ev.	64.3 \pm 0.0	64.7 \pm 2.1	62.9 \pm 1.9	61.6 \pm 3.0
	PySR	82.3	63.2	77.0	38.2
	FIM- ℓ ($w.n. = 2$)	69.0 \pm 0.0	67.0 \pm 0.8	77.5 \pm 0.9	76.1 \pm 1.3
	FIM- ℓ ($w.n. = 4$)	86.5 \pm 0.0	84.0 \pm 0.7	86.6 \pm 0.5	83.7 \pm 0.7
	FIM- ℓ (Weighted Sum)	100.0 \pm 0.0	96.9 \pm 0.4	97.2 \pm 1.2	93.1 \pm 1.2
1	ODEFormer Re-ev.	89.1 \pm 0.0	87.8 \pm 2.0	87.5 \pm 2.5	84.5 \pm 3.8
	FIM- ℓ ($w.n. = 2$)	97.8 \pm 0.0	93.5 \pm 0.0	98.7 \pm 1.1	93.9 \pm 1.7
	FIM- ℓ ($w.n. = 4$)	100.0 \pm 0.0	95.4 \pm 0.7	99.8 \pm 0.7	95.2 \pm 0.9
	FIM- ℓ ($w.n. = 8$)	100.0 \pm 0.0	95.4 \pm 0.7	99.8 \pm 0.7	93.5 \pm 1.0
	FIM- ℓ ($w.n. = 16$)	100.0 \pm 0.0	93.7 \pm 0.7	100.0 \pm 0.0	91.7 \pm 1.4
2	ODEFormer Re-ev.	62.5 \pm 0.0	63.8 \pm 3.5	61.4 \pm 3.6	60.7 \pm 4.6
	FIM- ℓ ($w.n. = 2$)	62.5 \pm 0.0	61.4 \pm 1.2	80.0 \pm 2.0	80.5 \pm 2.7
	FIM- ℓ ($w.n. = 4$)	94.6 \pm 0.0	93.8 \pm 1.3	95.0 \pm 1.1	93.6 \pm 0.9
	FIM- ℓ ($w.n. = 8$)	100.0 \pm 0.0	98.6 \pm 0.8	99.3 \pm 1.2	97.5 \pm 0.9
	FIM- ℓ ($w.n. = 16$)	100.0 \pm 0.0	98.4 \pm 0.6	99.5 \pm 0.9	97.0 \pm 1.5
3	ODEFormer Re-ev.	10.0 \pm 0.0	13.1 \pm 3.7	9.4 \pm 3.2	12.5 \pm 4.7
	FIM- ℓ ($w.n. = 2$)	15.0 \pm 0.0	15.0 \pm 4.1	17.5 \pm 2.6	18.0 \pm 2.6
	FIM- ℓ ($w.n. = 4$)	30.0 \pm 0.0	27.0 \pm 2.6	30.0 \pm 0.0	26.5 \pm 2.4
	FIM- ℓ ($w.n. = 8$)	45.0 \pm 0.0	40.5 \pm 1.6	49.5 \pm 6.0	43.0 \pm 6.3
	FIM- ℓ ($w.n. = 16$)	100.0 \pm 0.0	95.0 \pm 0.0	84.0 \pm 6.1	74.5 \pm 6.9
4	ODEFormer Re-ev.	75.0 \pm 0.0	68.8 \pm 11.6	68.8 \pm 11.6	56.3 \pm 17.7
	FIM- ℓ ($w.n. = 2$)	100.0 \pm 0.0	100.0 \pm 0.0	100.0 \pm 0.0	100.0 \pm 0.0
	FIM- ℓ ($w.n. = 4$)	100.0 \pm 0.0	100.0 \pm 0.0	100.0 \pm 0.0	100.0 \pm 0.0
	FIM- ℓ ($w.n. = 8$)	100.0 \pm 0.0	100.0 \pm 0.0	100.0 \pm 0.0	100.0 \pm 0.0
	FIM- ℓ ($w.n. = 16$)	100.0 \pm 0.0	100.0 \pm 0.0	100.0 \pm 0.0	100.0 \pm 0.0

Table 10: ODEBench RMSE of FIM- ℓ for different numbers of windows, split by dimensions. The standard deviation is calculated across 10 samplings of the corruption schemes.

Dim.	Model	$\rho = 0$	$\rho = 0$	$\rho = 0.5$	$\rho = 0.5$
		$\gamma = 0$	$\gamma = 0.05$	$\gamma = 0$	$\gamma = 0.05$
All	ODEFormer Re-ev.	1.45440 \pm 0.0	1.49561 \pm 0.28744	1.61460 \pm 0.07631	1.55996 \pm 0.06814
	FIM- ℓ ($w.n. = 2$)	1.49276 \pm 0.0	1.53191 \pm 0.01379	1.11169 \pm 0.02296	1.17046 \pm 0.02488
	FIM- ℓ ($w.n. = 4$)	0.89672 \pm 0.0	0.97397 \pm 0.00758	0.7747 \pm 0.01644	0.86858 \pm 0.01461
	FIM- ℓ ($w.n. = 8$)	0.47344 \pm 0.0	0.57404 \pm 0.0068	0.4351 \pm 0.00907	0.58163 \pm 0.01079
	FIM- ℓ ($w.n. = 16$)	0.14572 \pm 0.0	0.30887 \pm 0.0059	0.28492 \pm 0.020	0.52077 \pm 0.01884
	FIM- ℓ (Weighted Sum)	0.14572 \pm 0.0	0.25858 \pm 0.0059	0.28492 \pm 0.020	0.41192 \pm 0.0205
1	ODEFormer Re-ev.	0.50954 \pm 0.0	0.52900 \pm 0.13294	0.58829 \pm 0.04373	0.66961 \pm 0.09289
	FIM- ℓ ($w.n. = 2$)	0.47952 \pm 0.0	0.54023 \pm 0.01949	0.12225 \pm 0.00566	0.26812 \pm 0.01323
	FIM- ℓ ($w.n. = 4$)	0.03913 \pm 0.0	0.22905 \pm 0.01549	0.04358 \pm 0.00269	0.27359 \pm 0.01662
	FIM- ℓ ($w.n. = 8$)	0.02668 \pm 0.0	0.27605 \pm 0.01472	0.0215 \pm 0.00217	0.36447 \pm 0.01162
	FIM- ℓ ($w.n. = 16$)	0.01135 \pm 0.0	0.36661 \pm 0.01394	0.01218 \pm 0.00091	0.54251 \pm 0.01067
2	ODEFormer Re-ev.	0.58488 \pm 0.0	0.55307 \pm 0.05853	0.87805 \pm 0.12628	0.67336 \pm 0.17509
	FIM- ℓ ($w.n. = 2$)	0.48285 \pm 0.0	0.4882 \pm 0.003	0.33043 \pm 0.019	0.3402 \pm 0.02128
	FIM- ℓ ($w.n. = 4$)	0.14509 \pm 0.0	0.15864 \pm 0.00224	0.13071 \pm 0.01099	0.15387 \pm 0.01138
	FIM- ℓ ($w.n. = 8$)	0.04052 \pm 0.0	0.06608 \pm 0.00199	0.04881 \pm 0.00897	0.09019 \pm 0.00698
	FIM- ℓ ($w.n. = 16$)	0.00857 \pm 0.0	0.06297 \pm 0.00327	0.03812 \pm 0.01606	0.10932 \pm 0.00977
3	ODEFormer Re-ev.	6.34598 \pm 0.0	6.65072 \pm 1.60730	6.35373 \pm 0.32882	6.39117 \pm 0.38931
	FIM- ℓ ($w.n. = 2$)	6.94523 \pm 0.0	7.03731 \pm 0.07836	5.79548 \pm 0.14598	5.80209 \pm 0.14687
	FIM- ℓ ($w.n. = 4$)	5.15268 \pm 0.0	5.16363 \pm 0.02147	4.41386 \pm 0.0952	4.4104 \pm 0.09807
	FIM- ℓ ($w.n. = 8$)	2.8077 \pm 0.0	2.79512 \pm 0.01428	2.5547 \pm 0.05278	2.57153 \pm 0.06213
	FIM- ℓ ($w.n. = 16$)	0.86784 \pm 0.0	0.92454 \pm 0.0055	1.65999 \pm 0.13815	1.72432 \pm 0.12407
4	ODEFormer Re-ev.	0.03579 \pm 0.0	0.03170 \pm 0.00393	0.03305 \pm 0.00303	0.05530 \pm 0.03747
	FIM- ℓ ($w.n. = 2$)	0.02153 \pm 0.0	0.0213 \pm 0.00116	0.00883 \pm 0.00169	0.01288 \pm 0.00156
	FIM- ℓ ($w.n. = 4$)	0.00213 \pm 0.0	0.00696 \pm 0.00064	0.00247 \pm 0.0009	0.00786 \pm 0.00079
	FIM- ℓ ($w.n. = 8$)	0.00079 \pm 0.0	0.00715 \pm 0.00041	0.00147 \pm 0.00065	0.00961 \pm 0.00046
	FIM- ℓ ($w.n. = 16$)	0.00046 \pm 0.0	0.00917 \pm 0.00033	0.00121 \pm 0.00063	0.01318 \pm 0.0007

Table 11: ODEBench MAE of FIM- ℓ for different numbers of windows, split by dimensions. The standard deviation is calculated across 10 samplings of the corruption schemes.

Dim.	Model	$\rho = 0$	$\rho = 0$	$\rho = 0.5$	$\rho = 0.5$
		$\gamma = 0$	$\gamma = 0.05$	$\gamma = 0$	$\gamma = 0.05$
All	ODEFormer Re-ev.	1.06575 \pm 0.0	1.08829 \pm 0.15297	1.17828 \pm 0.05353	1.15633 \pm 0.04795
	FIM- ℓ ($w.n. = 2$)	1.13792 \pm 0.0	1.16799 \pm 0.00904	0.83951 \pm 0.01965	0.88588 \pm 0.01983
	FIM- ℓ ($w.n. = 4$)	0.65753 \pm 0.0	0.71483 \pm 0.00482	0.57207 \pm 0.01368	0.64132 \pm 0.01129
	FIM- ℓ ($w.n. = 8$)	0.33755 \pm 0.0	0.41024 \pm 0.00456	0.30721 \pm 0.00521	0.41284 \pm 0.00723
	FIM- ℓ ($w.n. = 16$)	0.09628 \pm 0.0	0.21383 \pm 0.00345	0.17416 \pm 0.01029	0.34229 \pm 0.01006
1	ODEFormer Re-ev.	0.32923 \pm 0.0	0.34722 \pm 0.08502	0.39660 \pm 0.04165	0.47208 \pm 0.04834
	FIM- ℓ ($w.n. = 2$)	0.38708 \pm 0.0	0.43727 \pm 0.01308	0.09335 \pm 0.00506	0.20900 \pm 0.01057
	FIM- ℓ ($w.n. = 4$)	0.02499 \pm 0.0	0.16663 \pm 0.01033	0.03213 \pm 0.00204	0.20268 \pm 0.01535
	FIM- ℓ ($w.n. = 8$)	0.02040 \pm 0.0	0.20011 \pm 0.01021	0.01403 \pm 0.00093	0.26112 \pm 0.01003
	FIM- ℓ ($w.n. = 16$)	0.00801 \pm 0.0	0.26645 \pm 0.00826	0.00692 \pm 0.00025	0.38727 \pm 0.00971
2	ODEFormer Re-ev.	0.40630 \pm 0.0	0.39648 \pm 0.03423	0.60159 \pm 0.07357	0.46471 \pm 0.09784
	FIM- ℓ ($w.n. = 2$)	0.33846 \pm 0.0	0.34071 \pm 0.00229	0.22632 \pm 0.01166	0.23367 \pm 0.01281
	FIM- ℓ ($w.n. = 4$)	0.08653 \pm 0.0	0.09716 \pm 0.00135	0.07813 \pm 0.00575	0.09487 \pm 0.00607
	FIM- ℓ ($w.n. = 8$)	0.02190 \pm 0.0	0.03982 \pm 0.00074	0.02557 \pm 0.00285	0.05379 \pm 0.00249
	FIM- ℓ ($w.n. = 16$)	0.00485 \pm 0.0	0.03821 \pm 0.00141	0.01548 \pm 0.00371	0.06106 \pm 0.00213
3	ODEFormer Re-ev.	4.81377 \pm 0.0	4.94279 \pm 0.82914	4.82151 \pm 0.18451	4.88917 \pm 0.31551
	FIM- ℓ ($w.n. = 2$)	5.32823 \pm 0.0	5.39580 \pm 0.05009	4.43940 \pm 0.12939	4.44416 \pm 0.12705
	FIM- ℓ ($w.n. = 4$)	3.84243 \pm 0.0	3.84711 \pm 0.01762	3.31108 \pm 0.08397	3.30732 \pm 0.08331
	FIM- ℓ ($w.n. = 8$)	2.01825 \pm 0.0	2.01172 \pm 0.01012	1.83143 \pm 0.03501	1.84830 \pm 0.04210
	FIM- ℓ ($w.n. = 16$)	0.57452 \pm 0.0	0.62605 \pm 0.00421	1.03782 \pm 0.07042	1.09290 \pm 0.06818
4	ODEFormer Re-ev.	0.02798 \pm 0.0	0.02361 \pm 0.00258	0.02508 \pm 0.00251	0.04356 \pm 0.03045
	FIM- ℓ ($w.n. = 2$)	0.01355 \pm 0.0	0.01418 \pm 0.00045	0.00539 \pm 0.00113	0.00960 \pm 0.00129
	FIM- ℓ ($w.n. = 4$)	0.00132 \pm 0.0	0.00531 \pm 0.00054	0.00131 \pm 0.00037	0.00588 \pm 0.00061
	FIM- ℓ ($w.n. = 8$)	0.00046 \pm 0.0	0.00511 \pm 0.00030	0.00066 \pm 0.00020	0.00685 \pm 0.00037
	FIM- ℓ ($w.n. = 16$)	0.00027 \pm 0.0	0.00650 \pm 0.00017	0.00053 \pm 0.00017	0.00933 \pm 0.00041

Table 12: ODEBench RMSE of the inferred time derivative of FIM- ℓ for different number of window, split by dimensions. The standard deviation is calculated across 10 samplings of the corruption schemes.

Dim.	Model	$\rho = 0$	$\rho = 0$	$\rho = 0.5$	$\rho = 0.5$
		$\gamma = 0$	$\gamma = 0.05$	$\gamma = 0$	$\gamma = 0.05$
All	ODEFormer (g.t. traj.)	30.49650 \pm 0.0	71.30478 \pm 131.29482	69.50647 \pm 50.34435	93.24899 \pm 105.60553
	ODEFormer (inf. traj.)	16.50882 \pm 0.0	13.10672 \pm 2.30755	19.82354 \pm 2.94507	17.77896 \pm 4.61146
	FIM- ℓ ($w.n. = 2$)	10.09833 \pm 0.0	10.07751 \pm 0.01023	9.80062 \pm 0.00628	9.85593 \pm 0.00853
	FIM- ℓ ($w.n. = 4$)	8.92481 \pm 0.0	9.01273 \pm 0.01408	8.74446 \pm 0.01624	8.89065 \pm 0.01899
	FIM- ℓ ($w.n. = 8$)	6.84601 \pm 0.0	7.177 \pm 0.03336	6.91584 \pm 0.03868	7.46845 \pm 0.04305
	FIM- ℓ ($w.n. = 16$)	3.49679 \pm 0.0	4.79098 \pm 0.06319	4.46558 \pm 0.13783	6.48983 \pm 0.17314
	FIM- ℓ (Weighted Sum)	3.49679 \pm 0.0	3.78833 \pm 0.0204	4.46558 \pm 0.1321	4.78349 \pm 0.136708
1	ODEFormer (g.t. traj.)	8.58175 \pm 0.0	6.98587 \pm 5.39939	23.63005 \pm 18.09459	20.6331 \pm 28.93572
	ODEFormer (inf. traj.)	6.21711 \pm 0.0	4.46383 \pm 2.4357	11.4018 \pm 5.99679	12.3632 \pm 9.90603
	FIM- ℓ ($w.n. = 2$)	0.57402 \pm 0.0	0.53237 \pm 0.02785	0.15242 \pm 0.00725	0.29413 \pm 0.02427
	FIM- ℓ ($w.n. = 4$)	0.08764 \pm 0.0	0.34632 \pm 0.03219	0.08866 \pm 0.00263	0.45892 \pm 0.04078
	FIM- ℓ ($w.n. = 8$)	0.06023 \pm 0.0	0.87099 \pm 0.08969	0.06783 \pm 0.00391	1.34817 \pm 0.10076
	FIM- ℓ ($w.n. = 16$)	0.04306 \pm 0.0	2.85851 \pm 0.14102	0.05609 \pm 0.00569	4.54185 \pm 0.25996
2	ODEFormer (g.t. traj.)	9.48347 \pm 0.0	115.23801 \pm 298.68335	9.06534 \pm 3.45804	100.57544 \pm 239.8902
	ODEFormer (inf. traj.)	1.29766 \pm 0.0	1.94693 \pm 2.33017	3.10378 \pm 2.06017	3.8734 \pm 3.27421
	FIM- ℓ ($w.n. = 2$)	1.43282 \pm 0.0	1.41955 \pm 0.00186	1.21969 \pm 0.01669	1.22876 \pm 0.01812
	FIM- ℓ ($w.n. = 4$)	0.70673 \pm 0.0	0.73517 \pm 0.00655	0.69129 \pm 0.03759	0.7396 \pm 0.03932
	FIM- ℓ ($w.n. = 8$)	0.21854 \pm 0.0	0.32851 \pm 0.01379	0.30857 \pm 0.04604	0.48065 \pm 0.05582
	FIM- ℓ ($w.n. = 16$)	0.09232 \pm 0.0	0.51666 \pm 0.03184	0.18537 \pm 0.03789	0.8219 \pm 0.06753
3	ODEFormer (g.t. traj.)	145.80444 \pm 0.0	110.45746 \pm 67.51671	358.12564 \pm 284.26566	258.31259 \pm 199.26659
	ODEFormer (inf. traj.)	86.05997 \pm 0.0	66.84346 \pm 9.40672	89.96053 \pm 10.58968	72.54148 \pm 24.72853
	FIM- ℓ ($w.n. = 2$)	58.27983 \pm 0.0	58.28185 \pm 0.00338	57.97466 \pm 0.0192	57.97117 \pm 0.01773
	FIM- ℓ ($w.n. = 4$)	54.04507 \pm 0.0	53.92284 \pm 0.01039	52.94947 \pm 0.05369	52.88163 \pm 0.0522
	FIM- ℓ ($w.n. = 8$)	42.37861 \pm 0.0	42.28708 \pm 0.03208	42.5487 \pm 0.21984	42.59756 \pm 0.22269
	FIM- ℓ ($w.n. = 16$)	21.67166 \pm 0.0	22.1478 \pm 0.09837	27.48439 \pm 0.82561	28.11654 \pm 0.85931
4	ODEFormer (g.t. traj.)	0.15883 \pm 0.0	0.14387 \pm 0.05189	0.16521 \pm 0.04465	0.44315 \pm 0.47787
	ODEFormer (inf. traj.)	0.0639 \pm 0.0	0.05313 \pm 0.01146	0.06529 \pm 0.01458	0.92522 \pm 2.12569
	FIM- ℓ ($w.n. = 2$)	0.03748 \pm 0.0	0.03646 \pm 0.00119	0.01764 \pm 0.00126	0.02066 \pm 0.00155
	FIM- ℓ ($w.n. = 4$)	0.00423 \pm 0.0	0.0116 \pm 0.00102	0.00546 \pm 0.00084	0.01556 \pm 0.00131
	FIM- ℓ ($w.n. = 8$)	0.00385 \pm 0.0	0.0245 \pm 0.00234	0.00529 \pm 0.00078	0.03523 \pm 0.00243
	FIM- ℓ ($w.n. = 16$)	0.00288 \pm 0.0	0.0707 \pm 0.00488	0.00366 \pm 0.00053	0.10899 \pm 0.00559

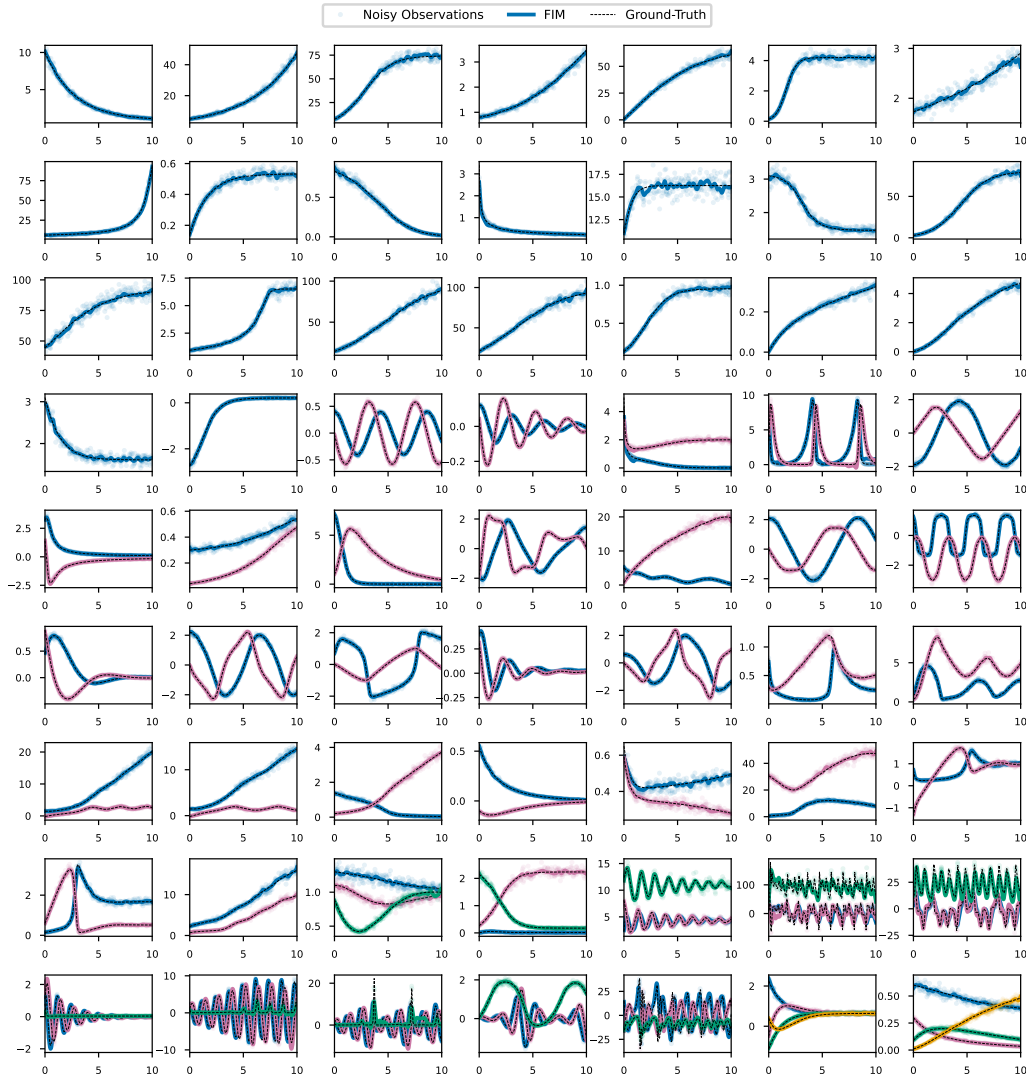


Figure 6: Reconstruction from noisy observations (dots) of all equations in the ODEBench dataset, using the first set of initial conditions, with corruptions $\rho = 0.5$ and $\gamma = 0.05$. $\text{FIM-}\ell$ (line) recovers the ground truth path (dashed line) closely for (almost) all equations.

Table 13: ODEBench MAE of the inferred time derivative of $FIM-\ell$ for different numbers of windows, split by dimensions. The standard deviation is calculated across 10 samplings of the corruption schemes.

Dim.	Model	$\rho = 0$	$\rho = 0$	$\rho = 0.5$	$\rho = 0.5$
		$\gamma = 0$	$\gamma = 0.05$	$\gamma = 0$	$\gamma = 0.05$
All	ODEFormer (g.t. traj.)	9.98246 \pm 0.0	10.3509 \pm 5.12400	11.43592 \pm 3.89992	14.56629 \pm 5.62873
	ODEFormer (inf. traj.)	7.47623 \pm 0.0	7.59557 \pm 0.80806	8.03686 \pm 0.38837	7.87698 \pm 0.61724
	$FIM-\ell(w.n. = 2)$	6.71538 \pm 0.0	6.71455 \pm 0.00866	6.47138 \pm 0.00666	6.51303 \pm 0.00678
	$FIM-\ell(w.n. = 4)$	5.86143 \pm 0.0	5.92169 \pm 0.00801	5.64520 \pm 0.01431	5.74910 \pm 0.01754
	$FIM-\ell(w.n. = 8)$	4.21719 \pm 0.0	4.45152 \pm 0.01683	4.21716 \pm 0.01543	4.58770 \pm 0.02492
	$FIM-\ell(w.n. = 16)$	1.90556 \pm 0.0	2.75833 \pm 0.03090	2.44375 \pm 0.05500	3.79191 \pm 0.04925
1	ODEFormer (g.t. traj.)	1.02333 \pm 0.0	0.85939 \pm 0.28399	1.93692 \pm 0.79555	1.69855 \pm 1.37894
	ODEFormer (inf. traj.)	1.22521 \pm 0.0	0.97085 \pm 0.44759	1.79378 \pm 0.60934	1.74534 \pm 1.01677
	$FIM-\ell(w.n. = 2)$	0.35084 \pm 0.0	0.35811 \pm 0.02167	0.06987 \pm 0.00370	0.17388 \pm 0.01507
	$FIM-\ell(w.n. = 4)$	0.03440 \pm 0.0	0.21994 \pm 0.01723	0.02992 \pm 0.00100	0.29445 \pm 0.02783
	$FIM-\ell(w.n. = 8)$	0.01847 \pm 0.0	0.57124 \pm 0.04161	0.02071 \pm 0.00083	0.85952 \pm 0.04000
	$FIM-\ell(w.n. = 16)$	0.01120 \pm 0.0	1.83930 \pm 0.07291	0.01563 \pm 0.00059	2.98943 \pm 0.12402
2	ODEFormer (g.t. traj.)	1.11424 \pm 0.0	4.60410 \pm 9.66290	1.25932 \pm 0.11240	4.67499 \pm 7.50841
	ODEFormer (inf. traj.)	0.55929 \pm 0.0	0.62367 \pm 0.29012	0.73061 \pm 0.14608	0.80667 \pm 0.31722
	$FIM-\ell(w.n. = 2)$	0.78924 \pm 0.0	0.78135 \pm 0.00215	0.59850 \pm 0.00569	0.60812 \pm 0.00550
	$FIM-\ell(w.n. = 4)$	0.33064 \pm 0.0	0.35679 \pm 0.00296	0.29782 \pm 0.00601	0.33816 \pm 0.00718
	$FIM-\ell(w.n. = 8)$	0.08201 \pm 0.0	0.15581 \pm 0.00496	0.10640 \pm 0.00910	0.21536 \pm 0.01454
	$FIM-\ell(w.n. = 16)$	0.02903 \pm 0.0	0.26067 \pm 0.01393	0.05549 \pm 0.00629	0.41416 \pm 0.01805
3	ODEFormer (g.t. traj.)	57.40099 \pm 0.0	50.32888 \pm 20.88564	64.04977 \pm 24.41574	74.73737 \pm 25.89933
	ODEFormer (inf. traj.)	42.71272 \pm 0.0	43.86978 \pm 4.69668	44.45747 \pm 2.04799	43.33972 \pm 3.66024
	$FIM-\ell(w.n. = 2)$	39.28646 \pm 0.0	39.28669 \pm 0.00501	38.93203 \pm 0.04304	38.92776 \pm 0.04075
	$FIM-\ell(w.n. = 4)$	35.92175 \pm 0.0	35.80043 \pm 0.01442	34.66166 \pm 0.08952	34.59348 \pm 0.08569
	$FIM-\ell(w.n. = 8)$	26.29593 \pm 0.0	26.29148 \pm 0.01758	26.22219 \pm 0.10493	26.31823 \pm 0.09887
	$FIM-\ell(w.n. = 16)$	11.89775 \pm 0.0	12.40848 \pm 0.03408	15.20400 \pm 0.34251	15.83980 \pm 0.32635
4	ODEFormer (g.t. traj.)	0.07487 \pm 0.0	0.0685 \pm 0.02815	0.07772 \pm 0.01916	0.16812 \pm 0.1964
	ODEFormer (inf. traj.)	0.01773 \pm 0.0	0.01533 \pm 0.00195	0.01658 \pm 0.00155	0.06136 \pm 0.09291
	$FIM-\ell(w.n. = 2)$	0.01824 \pm 0.0	0.01785 \pm 0.00047	0.00565 \pm 0.0006	0.00828 \pm 0.00107
	$FIM-\ell(w.n. = 4)$	0.00178 \pm 0.0	0.00667 \pm 0.00026	0.00179 \pm 0.0001	0.00892 \pm 0.00061
	$FIM-\ell(w.n. = 8)$	0.00135 \pm 0.0	0.01492 \pm 0.00074	0.00168 \pm 0.00008	0.02200 \pm 0.00134
	$FIM-\ell(w.n. = 16)$	0.00117 \pm 0.0	0.04355 \pm 0.00189	0.00143 \pm 0.00005	0.06961 \pm 0.00279

E.4 LORENZ SYSTEM AND LATENTODE

E.4.1 DATA DESCRIPTION AND PRE-PROCESSING

To compare our zero-shot model to a LatentODE, a specialised black-box model requiring training, we consider the chaotic Lorenz system

$$\begin{aligned} dx &= \sigma(y - x) \\ dy &= \rho x - y - xz \\ dz &= xy - \beta z \end{aligned}$$

with parameters $(\sigma, \beta, \rho) = (10, 28, \frac{8}{3})$. We simulate the system in the time interval $[0, 10]$, starting with initial values sampled from $\mathcal{N}([2.3, 8.1, 12.4], 1)$. Note that the Lorenz system with these parameters and the mean initial value is part of the ODEBench dataset.

To generate a time series, we sample an initial value, simulate the system and observe it at the regular grid on $[0, 1]$ with 512 points. The observations are subsampled with a survival probability of 0.5 and corrupted with additive gaussian noise sampled from $\mathcal{N}(0, 0.05)$.

We generate 1024 time series for the training of LatentODE and additional 128 time series each for validation and test.

E.4.2 TRAINING LATENTODE

We train LatentODE (Rubanova et al., 2019) on the standardised train set, selecting the model based on the lowest loss on the validation set. The encoder is an LSTM, the emission model a diagonal gaussian, fixing its standard deviation to 0.01. The target objective is the likelihood of the observations.

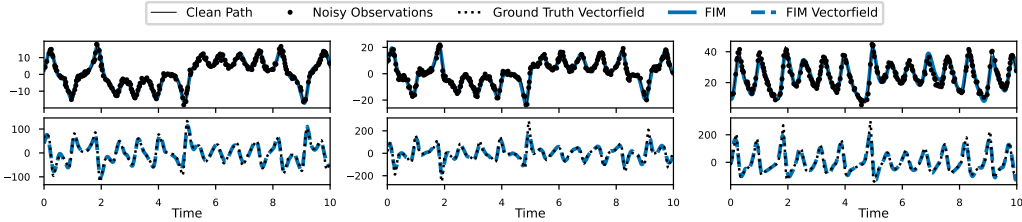


Figure 7: Inference of $\text{FIM-}\ell(w.n. = 16)$ on a Lorenz system time series, split into their individual dimensions. **(Top)** Noisy observations (black dots) of the system (black line) are interpolated by $\text{FIM-}\ell$ (blue line). **(Bottom)** Inferred values of the time derivative (blue dashed line) match the ground truth vector field values along the solution path (black dashed line) closely.

We train for 6000 epochs, with minibatches of size 32, using AdamW with learning rate $1e^{-3}$ and weight decay $1e^{-2}$. To help the model learn, we slowly anneal the input time series length over the initial 2000 epochs, starting at 25 observations.

We selected the model architecture by grid search. See Table 14 for the search grid and final parameters. The model trained roughly 9 hours on a A100 40GB GPU.

Table 14: Hyperparameters, including grid search range over some, for the LatentODE baseline on all datasets. Selected hyperparameters, determined by the loss on the validation set, are underlined. For simplicity, we set the dimension of the forward neural ODE to the hidden size of the encoder.

Hyperparameter	Lorenz System	Motion Capture	Navier Stokes
Hidden size	64, 128, 256	32, 64, 128	64, 128, 256
NeuralODE hidden layers	[64, 64], [128, 128]	[64, 64]	[128, 128]
Initial condition hidden layers	[64, 64], [128, 128]	[64, 64]	[128, 128]
Emission model hidden layers	[64, 64], [128, 128]	[64, 64]	[128, 128]

E.4.3 MODELLING AND RESULTS

Note that Latent ODE is notoriously difficult to train and we only managed to fit it to the data on a 64-dimensional hidden space (Dupont et al., 2019). The time derivative inference is therefore not directly feasible with our trained Latent ODE. We nevertheless compare $\text{FIM-}\ell(w.n. = 16)$ against said Latent ODE model on the reconstruction task, as well as against the Scipy⁸ implementation of the cubic spline.

Table 15 displays our results in terms of RMSE calculated against the ground-truth, clean solution path on all 512 of the regular grid. They averaged over the 128 trajectories in the test set for described data corruption scenario. $\text{FIM-}\ell$ not only outperforms both baselines, but also perfectly infers the hidden vector field along the solution path, as can be seen in Figure 7.

Table 15: Reconstruction task on the Lorenz system data. RMSE is calculated on the whole trajectory.

Model	Lorenz system
LatentODE	3.25 ± 0.99
Cubic spline	3.97 ± 5.8
$\text{FIM-}\ell$	2.01 ± 0.33

⁸<https://scipy.org/>

E.4.4 ABLATION STUDY: NUMBER OF WINDOWS

Additionally, we perform an ablation study on the numbers of windows processed by $\text{FIM-}\ell$ on the Lorenz test set.

Figure 8 shows the RMSE as the number of windows increases from 1 to 32.

Initially, the RMSE is considerably higher than the LatentODE baseline, demonstrating that $\text{FIM-}\ell$ on its own can not handle arbitrarily complex systems, because it has not been trained on such complex data. With the addition of more windows, the RMSE decreases sharply. However, beyond approximately 14 windows, the RMSE reduction tapers off, suggesting diminishing returns with further increases in the number of windows.

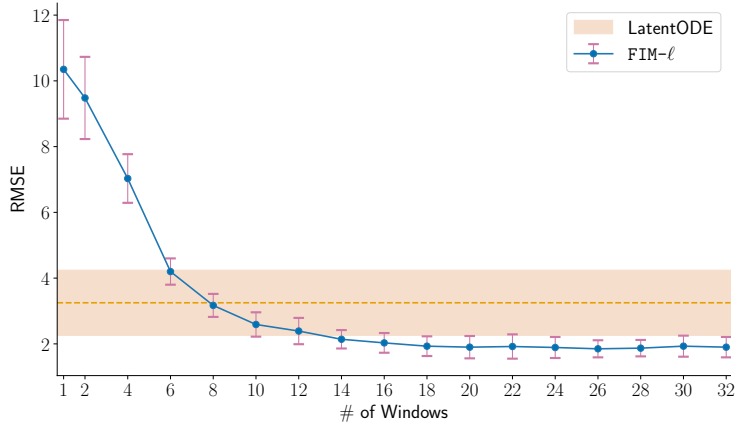


Figure 8: RMSE of LatentODE of $\text{FIM-}\ell(w.n. = m)$ for numbers of windows m between 1 and 32 on the Lorenz test set. The standard deviation across 128 time series is represented by the shaded area for the LatentODE and by the whiskers for each $\text{FIM-}\ell(w.n. = m)$. The performance of $\text{FIM-}\ell$ increases, as the number of windows increase.

E.5 COMPARISON AGAINST NEURAL ODE PROCESSES

E.5.1 DATA DESCRIPTION AND PRE-PROCESSING

Norcliffe et al. (2021) introduce four 1D synthetic datasets of different functional type, including sines, exponentials, straight lines, and harmonic oscillators. Each task is defined by a parameterized function, where the parameters are sampled from predefined uniform distributions. An example trajectory is generated by sampling from these parameter distributions and then sampling from the function at evenly spaced timestamps, t , over a fixed range to produce 100 data points (t, y) . The equations for these tasks, along with the ranges for their defining parameters, are provided in Table 16.

10 random context points are selected out of all 100 points. They serve as the model inputs, where the task is to reconstruct the original function at all 100 points.

Table 16: Description of functions considered by Norcliffe et al. (2021), including the mathematical form, ranges for parameters a and b , range for t , and the number of test samples.

Task	Form	a	b	t	# test
Sines	$y = a \sin(t - b)$	$(-1, 1)$	$(-1/2, 1/2)$	$(-\pi, \pi)$	10
Exponentials	$y = a/60 \times \exp(t - b)$	$(-1, 1)$	$(-1/2, 1/2)$	$(-1, 4)$	10
Straight lines	$y = at + b$	$(-1, 1)$	$(-1/2, 1/2)$	$(0, 5)$	10
Oscillators	$y = a \sin(t - b) \exp(-t/2)$	$(-1, 1)$	$(-1/2, 1/2)$	$(0, 5)$	10

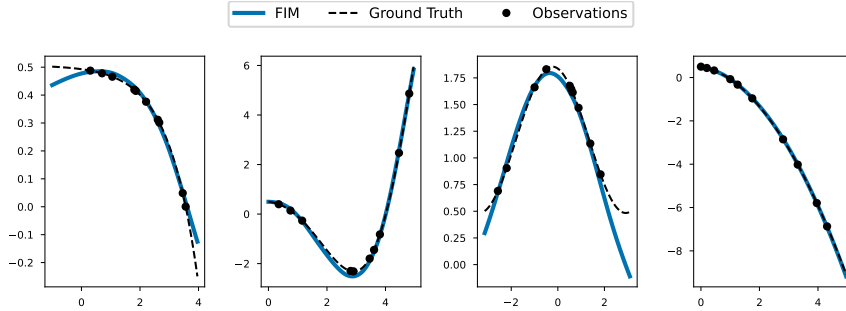


Figure 9: Samples from the one dimensional regression dataset of Norcliffe et al. (2021). The ground-truth path (black dashed lines) are observed at 10 irregular observation times (black dots). FIM- ℓ interpolates (blue line) well and recovers the ground-truth dynamics.

E.5.2 MODELLING AND RESULTS

In Table 17, we present the performance results of our pre-trained model FIM- $\ell(w.n. = 1)$ on the 1D Regression Task proposed by Norcliffe et al. (2021). MSE, MAE R^2 are calculated over all the points (not just a subset of the target points) for 10 different samples from each function type. The metrics from 10 samples per function type are averaged, and we report the mean and standard deviation.

It is important to reiterate that our model has not been trained on this dataset. Still, our model outperforms the baseline from Norcliffe et al. (2021) in three out of the four tasks. The Oscillator set is the only one where our model underperforms. Its trajectories exhibit rapid changes at the edges of the considered interval, which FIM- ℓ can not identify based solely on the sparse observations.

Figure 9 shows four samples from the test set and the corresponding inferences of our model.

Table 17: Results on the 1D regression dataset from Norcliffe et al. (2021). We report the mean and standard deviation over 10 samples of each function class. The Neural ODE Processes baselines are selected as the top performing model from Table 1 of Norcliffe et al. (2021).

Function	Model	$R^2 \uparrow$	MAE $\times 10^{-2} \downarrow$	MSE $\times 10^{-2} \downarrow$
Exponentials	Neural ODE Processes	-	-	0.25 \pm 0.04
	FIM- $\ell(w.n. = 1)$	0.9656 \pm 0.0079	1.11 \pm 0.11	0.07 \pm 0.02
Linear	Neural ODE Processes	-	-	3.16 \pm 0.76
	FIM- $\ell(w.n. = 1)$	0.9992 \pm 0.0002	3.85 \pm 0.47	0.34 \pm 0.09
Oscillators	Neural ODE Processes	-	-	0.55 \pm 0.03
	FIM- $\ell(w.n. = 1)$	0.8822 \pm 0.028	20.48 \pm 2.54	22.62 \pm 7.22
Sine	Neural ODE Processes	-	-	2.09 \pm 0.12
	FIM- $\ell(w.n. = 1)$	0.9679 \pm 0.0042	4.84 \pm 0.53	0.67 \pm 0.16

F POINT-WISE MISSING PATTERN IMPUTATION: ADDITIONAL RESULTS

F.1 COMPARING AGAINST BAYOTIDE

F.1.1 DATA DESCRIPTION AND PRE-PROCESSING

For the *point-wise missing pattern imputation* model, we first consider two available datasets from Fang et al. (2024a), namely the *Traffic-Guangzhou* and the *Solar* dataset.

Traffic-Guangzhou is a single time series with 500 observations and 214 components. *Solar* is a single time series with 52560 observations and 137 components.

For each of these datasets, the authors drop either 30% or 50% of the observed values. Importantly, components are dropped independent from each other, such that at any given observation time, components are (likely) only partially observed.

For our experiments, we use the pre-processed datasets provided by the authors⁹, including the sampled mask indicating dropped values.

F.1.2 MODELLING AND RESULTS

We apply $\text{FIM-}\ell(w.n. = m)$ with different number of windows m to both datasets and both observation ratios and compare our results to the baselines extracted from Tables 2 and 3 from Fang et al. (2024a).

Following the experimental setup of Fang et al. (2024a), we compute the metrics RMSE and MAE only at the missing values. Table 18 contains the results with an observation ratio of 50% and Table 19 the results for an observation ratio of 70%.

The two datasets are of vastly different lengths. Still, with a suitable number of windows, $\text{FIM-}\ell$ can impute the missing values well in both datasets. It even outperforms all available baselines, even though they have been trained on the datasets.

The center plot of Figure 3 displays a partial time series of one component of the *Traffic-Guangzhou* dataset, including the missing values and imputation by $\text{FIM-}\ell$. We can see that $\text{FIM-}\ell$ captures the local patterns well and uses them effectively to impute the missing values.

Table 18: Performance on two datasets from Fang et al. (2024a) with observed ratio 50%. Baselines have been extracted from Table 2 of Fang et al. (2024a). We highlight the overall best model per dataset in bold and underline our best-performing model.

Method	Traffic-GuangZhou		Solar-Power	
	RMSE	MAE	RMSE	MAE
SimpleMean	9.852	7.791	3.213	2.212
BRITS	4.874	3.335	2.842	1.985
NAOMI	5.986	4.543	2.918	2.112
SAITS	4.839	3.391	2.791	1.827
TIDER	4.708	3.469	1.679	0.838
Multi-Task GP	4.887	3.530	2.847	1.706
GP-VAE	4.844	3.419	3.720	1.810
CSDI	4.813	3.202	2.276	0.804
CSBI	4.790	3.182	2.097	1.033
BayOTIDE-fix weight	11.032	9.294	5.245	2.153
BayOTIDE-trend only	4.188	2.875	1.789	0.791
BayOTIDE	3.820	2.687	1.699	0.734
$\text{FIM-}\ell(w.n. = 1)$	10.614	8.113	-	-
$\text{FIM-}\ell(w.n. = 2)$	7.690	5.648	-	-
$\text{FIM-}\ell(w.n. = 4)$	5.377	3.861	-	-
$\text{FIM-}\ell(w.n. = 8)$	4.440	3.090	-	-
$\text{FIM-}\ell(w.n. = 16)$	3.741	2.562	-	-
$\text{FIM-}\ell(w.n. = 32)$	3.600	2.427	-	-
$\text{FIM-}\ell(w.n. = 800)$	-	-	2.044	1.188
$\text{FIM-}\ell(w.n. = 1600)$	-	-	1.667	0.755
$\text{FIM-}\ell(w.n. = 3200)$	-	-	1.550	0.595

F.2 COMPARING AGAINST SAITS

F.2.1 DATA DESCRIPTION AND PRE-PROCESSING

Du et al. (2023) collect four time series datasets (*PhysioNet-2012*, *Air-Quality*, *Electricity* and *ETT*) and benchmark a range of imputation models, including their own, on several imputation tasks. For detailed information about each of these datasets, including the sequence lengths and number of samples, we refer the reader to Table 1 of Du et al. (2023).

⁹<https://github.com/xuangu-fang/BayOTIDE>

Table 19: Performance on two datasets from Fang et al. (2024a) with observed ratio 70%. Baselines have been extracted from Table 3 of Fang et al. (2024a). We highlight the overall best model per dataset in bold and underline our best-performing model.

Method	Traffic-GuangZhou		Solar-Power	
	RMSE	MAE	RMSE	MAE
SimpleMean	10.141	8.132	3.156	2.319
BRITS	4.416	3.003	2.617	1.861
NAOMI	5.173	4.013	2.702	2.003
SAITS	4.407	3.025	2.359	1.575
TIDER	4.168	3.098	1.676	0.874
Multi-Task GP	4.471	3.223	2.618	1.418
GP-VAE	4.373	3.156	3.561	1.723
CSDI	4.301	2.991	2.132	1.045
CSBI	4.201	2.955	1.987	0.926
BayOTIDE-fix weight	13.319	9.290	5.238	2.026
BayOTIDE-trend only	4.002	2.759	1.651	0.712
BayOTIDE	3.724	2.611	1.621	0.709
FIM- $\ell(w.n. = 1)$	12.533	9.680	-	-
FIM- $\ell(w.n. = 2)$	9.020	6.810	-	-
FIM- $\ell(w.n. = 4)$	5.584	4.024	-	-
FIM- $\ell(w.n. = 8)$	4.401	3.084	-	-
FIM- $\ell(w.n. = 16)$	3.387	2.360	-	-
FIM- $\ell(w.n. = 32)$	3.087	2.148	-	-
FIM- $\ell(w.n. = 800)$	-	-	2.016	1.181
FIM- $\ell(w.n. = 1600)$	-	-	1.470	0.655
FIM- $\ell(w.n. = 3200)$	-	-	1.282	0.474

Here, we only consider one of their imputation tasks: point-wise imputation of 10% missing observations. The authors provide pre-processed datasets for this pattern¹⁰, which we use for the following evaluation. Note that their pre-processed data includes pre-sampled masks for the missing values, to enable a fair comparison to their results.

F.2.2 MODELLING AND RESULTS

Du et al. (2023) report MAE, RMSE and MRE for all datasets and a wide range of imputation models and methods in their Table 2, which we include here for completeness. We apply FIM- $\ell(w.n. = m)$ with different numbers of windows m and FIM- $\ell(o.n. = n)$ for different window lengths n to all datasets and report our results, together with the baselines, in Table 20.

With the right number or size of windows, FIM- ℓ is competitive on three out of four datasets. The *PhysioNet-2012* dataset is naturally sparse, where some components of a time series only contain a few observations. As a zero-shot approach that employs a channel independent strategy, FIM- ℓ does not perform well in such situations. In other words, *PhysioNet-2012* demonstrates the limitations of FIM- ℓ outlined in Appendix B.6.

F.3 TSI-BENCH

F.3.1 DATA DESCRIPTION AND PRE-PROCESSING

TSI-Bench is a collection of eight time series imputation datasets from different application domains: air-quality, traffic, energy and healthcare, assembled by Du et al. (2024). Its authors provide pre-processed splits of each dataset¹¹ for several imputation patterns.

Here, we consider their 10% and 50% point missing observation pattern. Note that the pre-processed datasets include sampled masks for missing values, enabling a fair comparison to their results.

¹⁰<https://github.com/WenjieDu/SAITS>

¹¹https://github.com/WenjieDu/Awesome_Imputation

Table 20: Performance on datasets from Du et al. (2023) with 10% imputation data. Baselines have been extracted from Table 2 of Du et al. (2023). We highlight the overall best model per dataset in bold and underline our best-performing model.

Method	PhysioNet-2012			Air-Quality			Electricity			ETT		
	MAE	RMSE	MRE	MAE	RMSE	MRE	MAE	RMSE	MRE	MAE	RMSE	MRE
Median	0.726	0.988	103.5%	0.763	1.175	107.4%	2.056	2.732	110.1%	1.145	1.847	139.1%
Last	0.862	1.207	123.0%	0.967	1.408	136.3%	1.006	1.533	53.9%	1.007	1.365	96.4%
GRUI-GAN	0.765	1.040	109.1%	0.788	1.179	111.0%	-	-	-	0.612	0.729	95.1%
E ² GAN	0.702	0.964	100.1%	0.750	1.126	105.6%	-	-	-	0.584	0.703	89.0%
M-RNN	0.533	0.776	76.0%	0.294	0.643	41.4%	1.244	1.867	66.6%	0.376	0.428	31.6%
GP-VAE	0.398	0.630	56.7%	0.268	0.614	37.7%	1.094	1.565	58.6%	0.274	0.307	15.5%
BRITS	0.256	0.767	36.5%	0.153	0.525	21.6%	0.847	1.322	45.3%	0.130	0.259	12.5%
Transformer	0.190	0.445	26.9%	0.158	0.521	22.3%	0.823	1.301	44.0%	0.114	0.173	10.9%
SAITS-base	0.192	0.439	27.3%	0.146	0.521	20.6%	0.822	1.221	44.0%	0.121	0.197	11.6%
SAITS	0.186	0.431	26.6%	0.137	0.518	19.3%	0.735	1.162	39.4%	0.092	0.139	8.8%
FIM- $\ell(w.n. = 1)$	0.443	0.899	63.3%	0.167	0.433	23.6%	0.118	0.251	6.3%	0.108	0.178	10.5%
FIM- $\ell(w.n. = 2)$	0.414	0.888	59.1%	0.146	0.414	20.7%	0.091	0.199	4.9%	<u>0.105</u>	<u>0.176</u>	<u>10.2%</u>
FIM- $\ell(w.n. = 4)$	0.406	0.849	58.0%	0.143	0.461	20.2%	0.078	0.174	4.2%	0.108	0.186	10.5%
FIM- $\ell(w.n. = 8)$	0.409	<u>0.751</u>	58.4%	0.186	0.541	26.0%	0.071	0.164	3.8%	0.134	0.252	13.0%
FIM- $\ell(w.n. = 16)$	0.479	0.842	68.5%	0.394	0.747	55.7%	0.070	0.162	3.7%	0.489	0.912	47.5%
FIM- $\ell(w.n. = 32)$	-	-	-	-	-	-	0.074	0.179	3.9%	-	-	-
FIM- $\ell(o.n. = 4)$	<u>0.364</u>	0.784	<u>52.0%</u>	0.137	0.438	19.3%	0.069	0.160	3.7%	0.106	0.184	10.3%
FIM- $\ell(o.n. = 6)$	0.483	1.047	69.0%	0.163	0.460	23.1%	0.126	0.329	6.6%	0.117	0.194	11.0%
FIM- $\ell(o.n. = 8)$	0.478	1.083	68.2%	0.165	0.443	23.3%	0.118	0.312	6.3%	0.114	0.195	11.1%
FIM- $\ell(o.n. = 12)$	0.461	1.048	65.8%	0.166	0.459	23.5%	0.114	0.288	6.1%	0.110	0.182	10.6%
FIM- $\ell(o.n. = 12)$	0.457	1.016	65.4%	0.165	0.447	23.3%	0.112	0.285	6.0%	0.109	0.182	10.6%
FIM- $\ell(o.n. = 16)$	0.453	0.987	64.7%	0.167	0.433	23.6%	0.111	0.271	6.0%	0.108	0.178	10.5%

For details about each individual time series dataset, including the pre-processing, we refer the reader to Appendix A of (Du et al., 2024).

F.3.2 MODELLING AND RESULTS

We apply FIM- $\ell(w.n. = m)$ with different numbers of windows m and FIM- $\ell(o.n. = n)$ for different window lengths n to all available datasets in both the 10% and 50% missingness patterns. In accordance with Du et al. (2024), we compute the performance metrics only at the missing values.

Table 21 contains the MAE of all baseline models (extracted from Table 2 of (Du et al., 2024)) and FIM- ℓ in the 10% missingness pattern. Table 22 contains the MAE and MSE of all baseline models (extracted from Table 11 of (Du et al., 2024)) and FIM- ℓ in the 50% missingness pattern.

Because of the short, and sometimes very sparse data (in particular in the 50% missingness pattern), we experimented with different application strategies for FIM- ℓ and report the corresponding results in both tables.

Let us now compare the two window specifying methods, FIM- $\ell(w.n. = m)$ and FIM- $\ell(o.n. = n)$ on the TSI-Bench datasets. Here, specifying the windows by their number of observations performs better overall, in particular in the 50% missingness pattern of Table 22. In the 10% missingness pattern, the (relative) difference between the two approaches is smaller, although still present.

With its windowing scheme, FIM- ℓ is not limited by the length of time series it can process. Some datasets in the TSI-Bench are based on a single long time series, that is split up into smaller chunks during pre-processing, to accommodate methods with such limitations. For these datasets, we experimented with *reassembling* the original time series via concatenation, before applying FIM- ℓ . We denote these models by Long-FIM- $\ell(w.n. = m)$.

The reassembled time series could provide more context for our zero-shot method to better extract the (local) patterns. Table 22 reveals that such strategy can indeed improve the performance, in particular in terms of the MSE. However, it does not improve the performance in all datasets and for all metrics.

Table 21: MAE on datasets from Du et al. (2024) with 10% point missingness. Baselines have been extracted from Table 2 of Du et al. (2024). Parenthesis indicate the standard deviation of five training rounds of neural models. We highlight the overall best model per dataset in bold and underline our best-performing model.

Method	BeijingAir	ItalyAir	PeMS	Pedestrian	ETT_h1	Electricity	PhysioNet2012	PhysioNet2019
iTransformer	0.123 (0.005)	0.223 (0.014)	0.226 (0.001)	0.148 (0.005)	0.263 (0.004)	0.571 (0.178)	0.379 (0.002)	0.462 (0.006)
SAITS	0.155 (0.004)	0.185 (0.010)	0.287 (0.001)	0.131 (0.006)	0.144 (0.006)	1.377 (0.026)	0.257 (0.019)	0.352 (0.005)
Nonstationary	0.209 (0.002)	0.266 (0.007)	0.331 (0.017)	0.453 (0.024)	0.359 (0.013)	0.213 (0.014)	0.410 (0.002)	0.458 (0.001)
ETSformer	0.187 (0.002)	0.259 (0.004)	0.347 (0.006)	0.207 (0.011)	0.227 (0.007)	0.412 (0.005)	0.373 (0.003)	0.451 (0.005)
PatchTST	0.198 (0.011)	0.274 (0.026)	0.330 (0.013)	0.126 (0.003)	0.240 (0.013)	0.550 (0.039)	0.301 (0.011)	0.420 (0.007)
Crossformer	0.184 (0.004)	0.246 (0.011)	0.337 (0.007)	0.119 (0.005)	0.232 (0.008)	0.540 (0.034)	0.525 (0.202)	0.378 (0.007)
Informr	0.148 (0.002)	0.205 (0.008)	0.302 (0.003)	0.154 (0.010)	0.167 (0.006)	1.291 (0.031)	0.297 (0.003)	0.403 (0.002)
Autoformer	0.257 (0.012)	0.295 (0.008)	0.598 (0.074)	0.197 (0.008)	0.267 (0.008)	0.748 (0.027)	0.417 (0.009)	0.476 (0.002)
Pyraformer	0.178 (0.004)	0.217 (0.006)	0.285 (0.003)	0.153 (0.012)	0.182 (0.008)	1.096 (0.033)	0.294 (0.002)	0.387 (0.004)
Transformer	0.142 (0.001)	0.191 (0.010)	0.294 (0.002)	0.136 (0.009)	0.178 (0.015)	1.316 (0.036)	0.259 (0.006)	0.341 (0.002)
BRITS	0.127 (0.001)	0.235 (0.007)	0.271 (0.000)	0.149 (0.005)	0.145 (0.002)	0.971 (0.016)	0.297 (0.001)	0.355 (0.001)
MRNN	0.568 (0.002)	0.638 (0.003)	0.624 (0.000)	0.735 (0.001)	0.789 (0.019)	1.824 (0.005)	0.708 (0.029)	0.778 (0.015)
GRUD	0.233 (0.002)	0.368 (0.012)	0.355 (0.002)	0.204 (0.008)	0.325 (0.004)	0.976 (0.015)	0.450 (0.004)	0.471 (0.001)
TimesNet	0.230 (0.010)	0.280 (0.004)	0.312 (0.001)	0.157 (0.008)	0.254 (0.008)	1.011 (0.016)	0.353 (0.003)	0.394 (0.003)
MICN	0.203 (0.001)	0.283 (0.004)	0.281 (0.003)	-	0.267 (0.010)	0.392 (0.006)	0.378 (0.013)	0.461 (0.007)
SCINet	0.191 (0.011)	0.288 (0.010)	0.487 (0.101)	0.149 (0.012)	0.246 (0.019)	0.581 (0.015)	0.341 (0.005)	0.427 (0.002)
StemGNN	0.161 (0.002)	0.260 (0.008)	0.493 (0.079)	0.127 (0.006)	0.248 (0.012)	1.360 (0.078)	0.331 (0.001)	0.416 (0.002)
FreTS	0.211 (0.008)	0.273 (0.008)	0.396 (0.027)	0.138 (0.004)	0.262 (0.029)	0.718 (0.043)	0.315 (0.008)	0.406 (0.017)
Koopa	0.363 (0.108)	0.307 (0.041)	0.532 (0.122)	0.173 (0.020)	0.435 (0.132)	1.309 (0.531)	0.413 (0.007)	0.451 (0.019)
DLinear	0.215 (0.016)	0.242 (0.009)	0.362 (0.009)	0.179 (0.004)	0.227 (0.006)	0.519 (0.008)	0.370 (0.000)	0.432 (0.001)
FILM	0.318 (0.010)	0.340 (0.011)	0.784 (0.064)	0.413 (0.010)	0.583 (0.008)	0.834 (0.031)	0.458 (0.001)	0.494 (0.003)
CSDI	0.102 (0.010)	0.539 (0.418)	0.238 (0.047)	0.231 (0.064)	0.151 (0.008)	1.483 (0.459)	0.252 (0.002)	0.408 (0.019)
US-GAN	0.137 (0.002)	0.264 (0.012)	0.296 (0.001)	0.151 (0.016)	0.458 (0.590)	0.938 (0.009)	0.310 (0.003)	0.358 (0.002)
GP-VAE	0.240 (0.006)	0.369 (0.012)	0.341 (0.007)	0.319 (0.010)	0.329 (0.017)	1.152 (0.074)	0.445 (0.006)	0.562 (0.004)
Mean	0.721	0.574	0.798	0.728	0.737	0.422	0.708	0.762
Median	0.681	0.518	0.778	0.667	0.710	0.408	0.690	0.747
LOCF	0.188	0.233	0.375	0.257	0.315	0.104	0.449	0.478
Linear	0.112	0.135	0.211	0.167	0.197	0.065	0.366	0.387
FIM- ℓ ($w.n. = 1$)	0.148	0.162	0.317	0.234	0.344	0.105	0.489	0.448
FIM- ℓ ($w.n. = 2$)	0.131	0.150	0.247	0.194	0.263	0.088	0.460	0.434
FIM- ℓ ($w.n. = 4$)	0.127	0.196	0.227	<u>0.170</u>	0.234	0.078	0.444	0.436
FIM- ℓ ($w.n. = 8$)	0.165	0.416	0.311	0.245	0.234	0.072	0.445	0.464
FIM- ℓ ($w.n. = 16$)	0.401	-	0.484	0.449	0.291	0.071	0.521	0.538
FIM- ℓ ($w.n. = 32$)	-	-	-	-	0.501	0.105	0.580	0.612
FIM- ℓ ($o.n. = 4$)	0.122	0.144	0.208	0.171	0.220	0.069	0.402	0.418
FIM- ℓ ($o.n. = 6$)	0.145	0.154	0.277	0.177	0.295	0.119	0.536	0.499
FIM- ℓ ($o.n. = 8$)	0.145	0.162	0.301	0.184	0.302	0.117	0.532	0.487
FIM- ℓ ($o.n. = 8$)	0.144	0.162	0.307	0.186	0.308	0.114	0.523	0.481
FIM- ℓ ($o.n. = 12$)	0.147	0.162	0.272	0.200	0.295	0.111	0.512	0.469
FIM- ℓ ($o.n. = 12$)	0.146	0.162	0.274	0.200	0.295	0.110	0.507	0.463
FIM- ℓ ($o.n. = 16$)	0.148	0.162	0.317	0.234	0.318	0.110	0.502	0.461
Long-FIM- ℓ ($w.n. = 16$)	-	0.425	-	-	-	-	-	-
Long-FIM- ℓ ($w.n. = 32$)	-	0.353	0.945	-	0.733	-	-	-
Long-FIM- ℓ ($w.n. = 64$)	0.397	0.235	0.705	-	0.495	-	-	-
Long-FIM- ℓ ($w.n. = 128$)	0.258	0.174	0.427	-	0.291	-	-	-
Long-FIM- ℓ ($w.n. = 256$)	0.167	0.145	0.273	-	0.240	0.172	-	-
Long-FIM- ℓ ($w.n. = 512$)	0.133	-	0.217	-	0.225	0.101	-	-
Long-FIM- ℓ ($w.n. = 1024$)	<u>0.120</u>	-	-	-	-	0.081	-	-
Long-FIM- ℓ ($w.n. = 2048$)	-	-	-	-	-	0.072	-	-
Long-FIM- ℓ ($w.n. = 4096$)	-	-	-	-	-	0.070	-	-

Table 22: MAE and MSE on datasets from Du et al. (2024) with 50% point missingness. Baselines have been extracted from Table 11 of Du et al. (2024). Parenthesis indicate the standard deviation of five training rounds of neural models. We highlight the overall best model per dataset in bold and underline our best-performing model.

Method	BeijingAir		ItalyAir		PeMS		ETT.h1		Electricity		Pedestrian	
	MAE	MSE	MAE	MSE	MAE	MSE	MAE	MSE	MAE	MSE	MAE	MSE
iTransformer	0.163 (0.003)	0.233 (0.004)	0.321 (0.007)	0.327 (0.011)	0.295 (0.007)	0.539 (0.016)	0.348 (0.002)	0.233 (0.003)	0.893 (0.085)	1.884 (0.160)	0.200 (0.006)	0.343 (0.006)
SAITS	0.194 (0.003)	0.193 (0.007)	0.285 (0.010)	0.236 (0.014)	0.302 (0.001)	0.595 (0.003)	0.223 (0.007)	0.107 (0.005)	1.399 (0.069)	3.837 (0.316)	0.205 (0.011)	0.392 (0.027)
Nonstationary	0.231 (0.001)	0.271 (0.007)	0.314 (0.005)	0.361 (0.010)	0.394 (0.013)	0.688 (0.016)	0.382 (0.004)	0.292 (0.006)	0.217 (0.031)	0.191 (0.048)	0.487 (0.033)	0.859 (0.098)
ETSformer	0.249 (0.004)	0.261 (0.009)	0.401 (0.007)	0.421 (0.011)	0.386 (0.007)	0.586 (0.009)	0.364 (0.013)	0.269 (0.022)	0.878 (0.008)	1.687 (0.024)	0.320 (0.004)	0.519 (0.010)
PatchTST	0.210 (0.009)	0.206 (0.007)	0.345 (0.011)	0.313 (0.010)	0.348 (0.006)	0.609 (0.008)	0.275 (0.023)	0.149 (0.017)	0.856 (0.044)	1.573 (0.141)	0.198 (0.003)	0.351 (0.005)
Crossformer	0.215 (0.007)	0.224 (0.004)	0.325 (0.009)	0.293 (0.009)	0.357 (0.003)	0.607 (0.008)	0.270 (0.021)	0.146 (0.017)	0.980 (0.344)	2.255 (1.656)	0.191 (0.008)	0.356 (0.014)
Informr	0.184 (0.005)	0.213 (0.003)	0.304 (0.007)	0.247 (0.015)	0.330 (0.005)	0.600 (0.009)	0.279 (0.008)	0.162 (0.007)	1.277 (0.028)	3.239 (0.080)	0.210 (0.006)	0.378 (0.021)
Autoformer	0.898 (0.001)	1.554 (0.003)	0.833 (0.017)	1.880 (0.044)	0.602 (0.068)	1.242 (0.173)	0.984 (0.008)	1.553 (0.025)	2.164 (0.001)	8.092 (0.010)	1.033 (0.015)	2.273 (0.082)
Pyraformer	0.198 (0.005)	0.223 (0.011)	0.312 (0.012)	0.254 (0.018)	0.305 (0.002)	0.580 (0.004)	0.291 (0.026)	0.167 (0.021)	1.131 (0.036)	2.711 (0.079)	0.202 (0.006)	0.381 (0.007)
Transformer	0.185 (0.003)	0.192 (0.005)	0.279 (0.011)	0.230 (0.017)	0.316 (0.004)	0.588 (0.005)	0.274 (0.012)	0.162 (0.017)	1.365 (0.034)	3.554 (0.085)	0.194 (0.014)	0.342 (0.033)
BRITS	0.169 (0.001)	0.194 (0.003)	0.321 (0.005)	0.283 (0.007)	0.287 (0.001)	0.561 (0.002)	0.238 (0.006)	0.127 (0.004)	1.124 (0.010)	2.828 (0.023)	0.259 (0.017)	0.433 (0.021)
MRNN	0.603 (0.006)	0.775 (0.006)	0.724 (0.001)	1.391 (0.006)	0.645 (0.001)	1.072 (0.003)	0.816 (0.006)	1.219 (0.004)	1.810 (0.004)	5.793 (0.011)	0.773 (0.001)	1.258 (0.003)
GRUD	0.279 (0.001)	0.303 (0.002)	0.476 (0.009)	0.539 (0.011)	0.372 (0.002)	0.619 (0.002)	0.417 (0.008)	0.337 (0.005)	1.087 (0.011)	2.458 (0.034)	0.307 (0.005)	0.507 (0.007)
TimesNet	0.265 (0.005)	0.233 (0.007)	0.370 (0.010)	0.323 (0.012)	0.348 (0.002)	0.567 (0.001)	0.339 (0.004)	0.210 (0.004)	1.131 (0.017)	2.644 (0.077)	0.269 (0.016)	0.392 (0.017)
MICN	0.456 (0.006)	0.553 (0.013)	0.548 (0.003)	0.852 (0.012)	0.392 (0.006)	0.608 (0.010)	0.606 (0.073)	0.688 (0.152)	0.965 (0.008)	2.018 (0.032)	-	-
SCINet	0.222 (0.012)	0.230 (0.036)	0.337 (0.008)	0.319 (0.006)	0.500 (0.093)	0.849 (0.193)	0.326 (0.014)	0.194 (0.013)	0.778 (0.023)	1.162 (0.115)	0.251 (0.005)	0.391 (0.015)
StemGNN	0.186 (0.004)	0.263 (0.005)	0.307 (0.014)	0.280 (0.019)	0.446 (0.021)	0.862 (0.064)	0.325 (0.019)	0.200 (0.025)	1.362 (0.187)	3.803 (0.920)	0.200 (0.009)	0.343 (0.014)
FreTS	0.235 (0.015)	0.246 (0.010)	0.349 (0.015)	0.345 (0.053)	0.422 (0.019)	0.686 (0.027)	0.319 (0.025)	0.195 (0.030)	0.871 (0.084)	1.320 (0.275)	0.224 (0.004)	0.314 (0.016)
Koopaa	0.373 (0.079)	0.445 (0.119)	0.345 (0.032)	0.359 (0.056)	0.506 (0.114)	0.855 (0.184)	0.515 (0.159)	0.577 (0.351)	1.755 (0.250)	7.390 (1.677)	0.246 (0.017)	0.330 (0.030)
DLinear	0.245 (0.005)	0.242 (0.006)	0.340 (0.004)	0.337 (0.005)	0.389 (0.013)	0.604 (0.020)	0.311 (0.003)	0.186 (0.003)	0.734 (0.011)	0.988 (0.038)	0.310 (0.002)	0.455 (0.006)
FILM	0.331 (0.009)	0.409 (0.009)	0.402 (0.018)	0.468 (0.052)	0.781 (0.059)	1.499 (0.124)	0.589 (0.005)	0.793 (0.003)	0.907 (0.024)	1.434 (0.078)	0.453 (0.007)	0.664 (0.008)
CSDI	0.144 (0.007)	0.472 (0.155)	0.958 (0.551)	29.266 (31.183)	0.288 (0.040)	0.651 (0.090)	0.318 (0.016)	0.207 (0.011)	0.798 (0.455)	21.850 (22.140)	0.351 (0.074)	1.117 (0.220)
US-GAN	0.192 (0.001)	0.187 (0.005)	0.357 (0.009)	0.278 (0.011)	0.330 (0.001)	0.566 (0.001)	0.755 (0.973)	2.119 (3.955)	1.119 (0.007)	2.610 (0.018)	0.233 (0.005)	0.328 (0.007)
GP-VAE	0.258 (0.004)	0.234 (0.008)	0.453 (0.014)	0.495 (0.022)	0.346 (0.015)	0.617 (0.015)	0.414 (0.013)	0.301 (0.011)	1.099 (0.032)	2.973 (0.040)	0.451 (0.022)	0.677 (0.031)
Mean	0.708	1.078	0.588	1.096	0.799	1.416	0.738	0.971	0.423	0.581	0.763	1.258
Median	0.677	1.143	0.533	1.116	0.777	1.476	0.708	1.022	0.408	0.627	0.705	1.386
LOCF	0.264	0.429	0.346	0.511	0.547	1.094	0.425	0.491	0.140	0.181	0.365	0.636
Linear	0.165	0.231	0.214	0.252	0.343	0.539	0.267	0.178	0.078	0.035	0.247	0.279
FIM- $\ell(w.n. = 1)$	0.198	0.325	0.254	0.287	0.496	0.960	0.411	0.370	0.110	0.057	0.343	0.366
FIM- $\ell(w.n. = 2)$	0.185	0.330	0.236	0.271	0.434	0.840	0.337	0.275	0.096	0.047	0.303	0.305
FIM- $\ell(w.n. = 4)$	0.190	0.371	0.352	0.609	0.384	0.714	0.317	0.251	0.093	0.045	<u>0.273</u>	0.251
FIM- $\ell(w.n. = 8)$	0.318	0.520	0.563	1.049	0.473	0.866	0.326	0.305	0.091	0.046	0.388	0.450
FIM- $\ell(w.n. = 16)$	0.559	0.886	-	-	0.626	1.136	0.445	0.508	0.122	0.140	0.574	0.763
FIM- $\ell(w.n. = 32)$	-	-	-	-	-	-	0.650	0.911	0.533	1.499	-	-
FIM- $\ell(o.n. = 4)$	0.166	0.298	0.225	0.249	0.375	0.708	0.279	0.198	0.083	0.038	0.274	0.272
FIM- $\ell(o.n. = 6)$	0.240	0.506	0.250	0.282	0.583	1.295	0.469	0.662	0.210	0.336	0.294	0.287
FIM- $\ell(o.n. = 8)$	0.234	0.422	0.254	0.287	0.583	1.327	0.467	0.661	0.199	0.294	0.306	0.314
FIM- $\ell(o.n. = 8)$	0.233	0.401	0.254	0.287	0.568	1.235	0.467	0.649	0.191	0.257	0.302	0.293
FIM- $\ell(o.n. = 12)$	0.208	0.370	0.254	0.287	0.533	1.098	0.420	0.453	0.187	0.227	0.327	0.334
FIM- $\ell(o.n. = 12)$	0.212	0.410	0.254	0.287	0.546	1.136	0.420	0.448	0.182	0.211	0.324	0.325
FIM- $\ell(o.n. = 16)$	0.198	0.325	0.254	0.287	0.496	0.960	0.417	0.500	0.198	0.240	0.343	0.366
Long-FIM- $\ell(w.n. = 16)$	-	-	0.414	0.458	-	-	-	-	-	-	-	-
Long-FIM- $\ell(w.n. = 32)$	-	-	0.358	0.383	0.905	1.692	0.693	1.084	-	-	-	-
Long-FIM- $\ell(w.n. = 64)$	0.360	0.512	0.283	0.282	0.709	1.193	0.495	0.576	-	-	-	-
Long-FIM- $\ell(w.n. = 128)$	0.266	0.397	0.238	0.245	0.516	0.848	0.362	0.303	-	-	-	-
Long-FIM- $\ell(w.n. = 256)$	0.201	0.279	<u>0.215</u>	<u>0.231</u>	0.417	0.721	0.328	0.281	0.157	0.103	-	-
Long-FIM- $\ell(w.n. = 512)$	0.177	<u>0.265</u>	-	-	<u>0.365</u>	<u>0.651</u>	0.310	0.265	0.106	0.052	-	-
Long-FIM- $\ell(w.n. = 1024)$	0.171	0.279	-	-	-	-	-	-	0.094	0.044	-	-
Long-FIM- $\ell(w.n. = 2048)$	-	-	-	-	-	-	-	-	0.089	0.043	-	-
Long-FIM- $\ell(w.n. = 4096)$	-	-	-	-	-	-	-	-	0.097	0.066	-	-

G TEMPORAL MISSING PATTERN IMPUTATION: ADDITIONAL RESULTS

G.1 MOTION CAPTURE

G.1.1 DATA DESCRIPTION AND PRE-PROCESSING

Let us now consider the imputation problem setup proposed by [Heinonen et al. \(2018\)](#) on a human motion capture dataset, consisting of 50-dimensional pose measurements of walking subjects. We take the data provided by [Yildiz et al. \(2019\)](#), which was pre-processed according to previous work of [Wang et al. \(2007\)](#).

The dataset contains 43 trajectories of a maximal length of 125. Following [Heinonen et al. \(2018\)](#), we remove 20% out of the center of each trajectory. To compare to [Heinonen et al. \(2018\)](#), we also apply the provided PCA projection and consider the first 3 PCA components. In the following, we call this the *PCA* setup.

Because FIM can be applied to arbitrary dimensional data, due to our channel independent strategy (see Appendix C.7), we also consider the 50 dimensional data directly. In the following, we call this the *No PCA* setup.

G.1.2 TRAINING LATENTODE

To obtain another baseline model, we train LatentODE ([Rubanova et al., 2019](#)) on the first 3 PCA components on the likelihood *outside* of the interpolation window, i.e. it has never seen and is not trained on the (missing) data *inside* the imputation window. We train and test on all 43 trajectories, selecting the model based on the performance on all trajectories. This approach is similar to the approach of models trained in [Heinonen et al. \(2018\)](#).

The training data is standardised for training. We use a LSTM as the encoder and a diagonal gaussian emission model, fixing its standard deviation to 0.01. We train for 120.000 gradient descent iterations over the whole dataset, using AdamW with learning rate $1e^{-3}$ and weight decay $1e^{-2}$. To help the model learn, we slowly anneal the input time series length over the initial 60.000 epochs, starting at 25 observations.

We did ablation over the hidden size of the model. See Table 14 for the final hyperparameters. The model trained roughly 3.5 hours on a A100 40GB GPU.

G.1.3 MODELLING AND RESULTS

In accordance with [Heinonen et al. \(2018\)](#), we compute the performance metrics in 50 dimensional space and only on the missing points inside the imputation gap. We evaluate FIM, LatentODE and also a cubic spline composed with Savitzky–Golay filters ([Savitzky & Golay, 1964](#)) in the *PCA* setup. Table 23 reports the RMSE, including baselines extracted from [Heinonen et al. \(2018\)](#), while Table 24 reports the MAE.

FIM performs almost as well as the specialized LatentODE model, especially when considering the large standard deviation for both approaches. These results indicate that a zero-shot imputation approach is indeed viable.

PCA dimensionality reduction induces some level of intrinsic error. In contrast to our baseline models, FIM is not restricted by dimensionality of the data. By applying our model to the 50 dimensional data *without PCA projection*, we can, in principle, avoid this error.

We report the results of this *No PCA* setup in Tables 23 and 24. Indeed, our model is performing better without the PCA projection, showcasing the strengths of our flexible, zero-shot methodology

Table 23: RMSE of imputation in the Motion Capture and Navier Stokes datasets. The RMSE is calculated only in the imputation window, in accordance with Heinonen et al. (2018).

Model	Filter	Motion Capture		Navier Stokes	
		PCA	No PCA	PCA	No PCA
LatentODE	-	3.066 ± 1.767	-	0.133 ± 0.053	-
Cubic spline	-	7.333 ± 2.49	8.95 ± 2.78	0.174 ± 0.003	0.186 ± 0.004
Cubic spline	Savgol(15, 3)	6.317 ± 1.813	6.752 ± 1.676	0.151 ± 0.003	0.143 ± 0.002
Cubic spline	Savgol(8, 3)	7.078 ± 2.147	8.271 ± 2.282	0.148 ± 0.003	0.147 ± 0.003
Cubic spline	Savgol(4, 3)	7.251 ± 2.184	8.783 ± 2.508	0.171 ± 0.003	0.18 ± 0.004
npODE	-	3.94 ± 3.50	-	-	-
GPDM	-	5.31 ± 3.39	-	-	-
VGPLVM	-	3.91 ± 1.89	-	-	-
FIM	-	3.271 ± 1.22	2.977 ± 0.96	0.103 ± 0.004	0.971 ± 0.005

Table 24: MAE of imputation in the Motion Capture and Navier Stokes datasets. The MAE is calculated only in the imputation window, in accordance with Heinonen et al. (2018).

Model	Filter	Motion Capture		Navier Stokes	
		PCA	No PCA	PCA	No PCA
LatentODE	-	1.658 ± 0.989	-	0.076 ± 0.03	-
Cubic spline	-	3.362 ± 1.175	4.209 ± 1.436	0.085 ± 0.003	0.083 ± 0.003
Cubic spline	Savgol(15, 3)	2.897 ± 0.871	2.998 ± 0.881	0.084 ± 0.00	0.075 ± 0.002
Cubic spline	Savgol(8, 3)	3.229 ± 1.029	3.695 ± 1.22	0.081 ± 0.003	0.072 ± 0.002
Cubic spline	Savgol(4, 3)	3.298 ± 1.035	4.061 ± 1.354	0.085 ± 0.003	0.082 ± 0.003
FIM	-	1.765 ± 0.627	1.611 ± 0.453	0.062 ± 0.003	0.051 ± 0.002

G.2 NAVIER STOKES

G.2.1 DATA DESCRIPTION AND PRE-PROCESSING

As an application of FIM to high-dimensional data, we consider the simulation of a two-dimensional, incompressible Navier-Stokes equation from (Course & Nair, 2023)¹². The equation is simulated on a two-dimensional grid of size 199×1499 for a total of 596,602 states. Following (Course & Nair, 2023), we remove the first 20% of the trajectory for warmup and are left with 2441 simulation steps.

We use this preprocessed simulation to create another imputation dataset, with a similar setup as in the motion capture dataset. We drop the last observation and cut the remaining trajectory into 61 time series of length 40. Then we remove the central 20% of each time series, creating a temporal missing pattern imputation task.

While our model can handle this high-dimensional data, as we will show below, we need to apply PCA dimensionality reduction to train a (specialized) baseline model. Following (Course & Nair, 2023), we project the data to 38 dimensional space with randomised PCA, which already captures the high dimensional dynamics well.

In the following, we will again refer to these two setups as *PCA* and *No PCA* respectively.

G.2.2 TRAINING LATENTODE

As a baseline, we train LatentODE (Rubanova et al., 2019) in the *PCA* setup on the likelihood *outside* of the imputation window, with the same reasoning as for the motion capture imputation problem in Section G.1.2.

LatentODE is trained on all 61 (standardised) time series, uses a LSTM as the encoder and a diagonal gaussian emission model with fixed standard deviation of 0.01. We train for 300,000 gradient descent iterations over the whole dataset, using AdamW with learning rate $1e^{-3}$ and weight decay

¹²<https://github.com/coursekevin/svis>

$1e^{-2}$. We slowly anneal the input time series length over the initial 60.000 epochs, starting at just 5 observations.

We studied some ablation over the hidden size. The search grid, including the final hyperparameters, is shown in Table Table 14. The model trained roughly 7 hours on a A100 40GB GPU.

G.2.3 MODELLING AND RESULTS

Let us first consider the *PCA* setup where we trained the LatentODE baseline. For both *FIM* and LatentODE we report the RMSE, in Table 23, and MAE, in Table 24, inside the imputation gap. In this particular task, *FIM* was again able to match the performance of LatentODE.

As *FIM* can be applied to data of any dimensionality, we also experimented with the *No PCA* setup, imputing the missing data in 596, 602 dimensional space directly. As in the Motion Capture dataset, *FIM* performs even better without the errors induced by the PCA projection.

Finally, we report the computational load of inference in dataset, as it is considerably larger than in all other experiments, because of its high dimensionality. The application of *FIM* took roughly 9 hours on a A100 40GB GPU. As a comparison, the application of a cubic spline on the same data took roughly 1.1 hours on 32 CPU cores.